Determination of the Degree of Ordering in the Modifier Cation Clustering in Silicate Glasses by ^{29}Si NMR and *Ab Initio* Calculations

THESIS

Presented in Partial Fulfillment of the Requirements for the Degree Bachelor of Science with Research Distinction in Chemistry at The Ohio State University

By

Eric George Keeler

* * * * *

The Ohio State University

2012

Thesis Committee:

Professor Christopher P. Jaroniec

Professor Philip J. Grandinetti, Adviser

Approved by

_____

Adviser

Department of Chemistry

ABSTRACT

New data is presented on mixed modified tetra-silicate glass of composition (1-z)$[K_{2x}Mg_{(1-x)}O \cdot 4SiO_2] \cdot zCuO$ where x = 1, 0.875, 0.75, 0.625, and 0.5, and z $\approx$ 0.004. This glass, with compositions of x = 1 and 0.5, was studied using ^{17}O dynamic-angle spinning (DAS) NMR in 1992 by Farnan and coworkers [1] and it was shown that there was considerable order of the non-bridging oxygen sites. The ^{29}Si sites were studied using two-dimensional magic angle flipping (2D MAF) NMR at natural abundance to examine the degree to which this clustering can be observed in a range of glass compositions. A chemical shift anisotropy, $\zeta_{\delta\ site\ 1}$, of -84.7 $\pm$ 0.1 ppm for the x = 1 sample and, $\zeta_{\delta\ site\ 2}$ of -60.4 $\pm$ 0.2 ppm for the x = 0.5 sample were determined based on a two site simulation of the MAF spectra. The chemical shift anisotropy of the x = 1 sample corresponds to a pure potassium coordination environment, whereas, the chemical shift anisotropy of the x = 0.5 sample corresponds to a mixed potassium/magnesium coordination environment, which is proposed as a $K_{2i} \cdot Mg_i$, where the potassium-to-magnesium ratio is believed to be restrictive but the total number of modifier cations near each non-bridging oxygen is not known. A three-site simulation was used to fit the other glass compositions. Two distinct anisotropic lineshapes were found with: $\zeta_{\delta\ site\ 1}$ = -85.5 $\pm$ 1.1 ppm and $\zeta_{\delta\ site\ 2}$ = -63.1 $\pm$ 4.8 ppm for the x = 0.875 sample, $\zeta_{\delta\ site\ 1}$ = -86.2 $\pm$ 0.4 ppm and $\zeta_{\delta\ site\ 2}$ = -58.6 $\pm$ 0.3 ppm for the x = 0.75 sample, and $\zeta_{\delta\ site\ 1}$ = -87.5 $\pm$ 0.6 ppm and $\zeta_{\delta\ site\ 2}$ = -61.9 $\pm$ 0.3 ppm for

the x = 0.625 sample. These sites correspond to the same cation clustering coordination environments from the x = 1 and x = 0.5 samples. *Ab initio* quantum chemical calculations were performed on a basic silicate tetrahedron built to emulate various $Q^{(n)}$-species with different Si-NBO bond distances to investigate the experimentally determined trend between the network modifying cation potential and the anisotropy of the clusters. Both the experimental results and theoretical *ab initio* calculations indicate that as cations with larger cation potentials are incorporated into the glass, the magnitude of the anisotropy increases.

I dedicate this thesis to my parents, Jeffery and Kristina Keeler.

ACKNOWLEDGMENTS

"Today is your day. You're off to Great Places! You're off and away!"

Oh, The Places You'll Go! ∼ Dr. Seuss

I would like to thank all of those people who have helped to guide my academic journey and whose guidance and advice have helped take me to the places that I have gone. I would especially like to thank my parents, Jeffery and Kristina Keeler, who have provided me with constant encouragement. I would also like to thank my sister, Danielle Keeler for showing me that college wasn't so terrible. I would also like to thank Alexandra for providing support for me throughout the process of writing my thesis. I would like to thank Dr. Ted M. Clark for beginning my path into scientific research. In addition, I would like to thank Dr. Jay H. Baltisberger whose unending advice and guidance have helped shape me into the researcher I am today. He has taught me more about scientific research in one year than I could have hoped to learn on my own. The rest of the Grandinetti lab also warrants mention for all of the work that they put in to make the research for this thesis happen. Finally, I would like to thank Dr. Philip J. Grandinetti for granting me the opportunity to not only conduct fascinating research but to also present it. His guidance and mentoring has taught me more than any class or book ever could. Without the guidance and foresight of those that have come before me I would not have succeeded in my goals. Therefore, I must thank all those who helped to pave my path to success.

TABLE OF CONTENTS

Page

LIST OF FIGURES

Figure **Page**

LIST OF TABLES

Table **Page**

CHAPTER 1

Introduction

1.1 Glass

1.1.1 History of Glass

Since early human history, glasses have had and continue to have great technological impact on our society, with applications such as drinking glasses, cookware, automotive windshields, laboratory apparatus, dental materials, and even nuclear waste containment [13–15]. The glassy state also plays an important role in natural geological processes, such as volcanism [13], and even in biological processes, such as anyhydrobiosis [16]. Volcanic glasses, such as obsidian, were first used by man to make weapons and tools [17–19]. Glasses were some of the earliest man-made materials and were first created in the Middle-East (Mesopotamia, Egypt, or Syria) approximately five thousand years ago [13, 20, 21]. Early glasses were cloudy and fragile due to the presence of metals within the glass structure [13, 22]. Glass was the first material that early man had the ability to produce with a given property (its color) by altering the composition at will [13]. Early glasses were reserved for royalty and used as jewels and amulets [13, 17]. The development of glassblowing, which made shaping and making glasses faster and less expensive, by the Ptolemies in the third century B.C., started an industrial revolution in glassmaking [13, 23, 24].

Glass making evolved over the next two thousand years into a major industry and was even integral in scientific advancement [13, 17, 19, 25].

1.1.2 Glass Formation and Definition

There are many different ways to define a glass [13, 19]. One particular definition states that glass formation is achieved by rapidly cooling a liquid into a super-cooled liquid-like state [14]. The rapid cooling, or quenching, does not allow the atoms and molecules in the liquid state to rearrange into a low energy crystalline solid state. This definition is somewhat restrictive as glasses can be formed from a solid or gas [26–34], from precipitation [35, 36], and even by electrolytic deposition [37, 38]. Therefore, to avoid dealing with these semantics, we will discuss the broader issue of atomic-level structure determination in non-crystalline solids, which include glasses [19]. Glasses are often described as amorphous solids implying that there is an atomic-level disorder within the glassy structure, although the extent of order and disorder is not well understood [14]. An improved understanding of the atomic-level structure of glass, and how this structure is correlated to properties would allow glasses to be designed for improved technological performance.

1.1.3 Structural Models of Glasses

Due to the disorder inherent in the glassy structure, atomic-level details about the structure of glasses have proven illusive [39–41]. Glass structure was first defined based on its short range bonding order, which is a central atom connected to ligands. Silicate glasses, for example, are known to be composed of a network of silicate tetrahedra [2] that are interlinked through bridging oxygen bonds as shown in Figure 1.1. As network-modifying cations are incorporated in the glass structure,

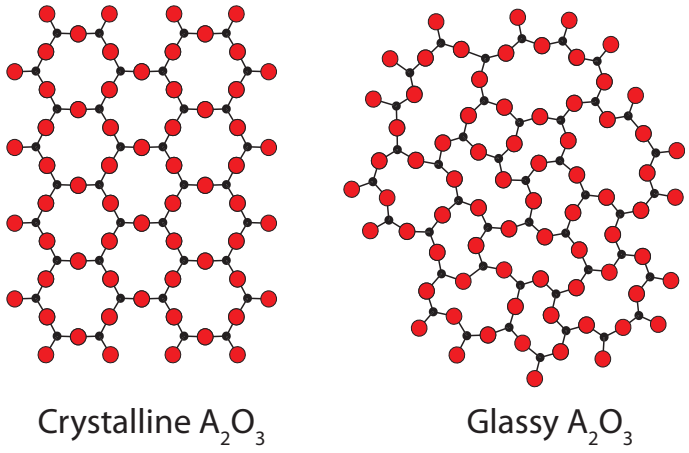

Figure 1.1: The structure of glass (right) from the model proposed by Zachariasen [2]. The glass structure is described as having local order but lacking long-range periodicity. The structure is shown in contrast to the structure of a crystalline solid (left), which contains long-range structural periodicity.

Si-O-Si bonds are broken to form non-bridging oxygen (NBO) sites [19] as shown in Figure 1.2. Therefore, the oxygen anions within the glass can be divided into two types, those that connect two silicate tetrahedra are called bridging oxygen (BO), and the terminal oxygens that coordinate to a network modifying cation, called non-brdging oxygen (NBO) sites. The distribution of these network modifying cations was first proposed to be ordered and to depolymerize the silicate structure throughout the glass structure by Zachariasen [2]. However, Warren and Briscoe studied the glass structure by X-ray diffraction (XRD) [3] and determined that their results led not to an ordered distribution of modifying cations within the glass structure, but to a random distribution of the modifying cations throughout the glass, as shown in Figure 1.3.

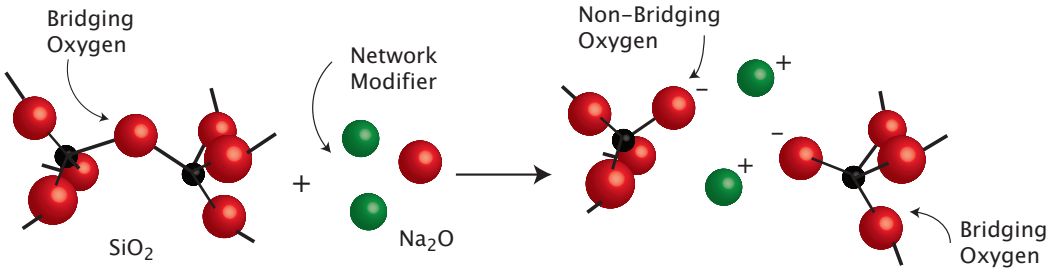

Figure 1.2: When a network modifying cation is introduced into the glass, Na^+ is shown, the bridging oxygen (BO) sites within the glass structure are broken. The terminating oxygen sites within the glass are called non-bridging oxygen (NBO) sites. The network modifying cations cluster near the NBO sites within the glass.

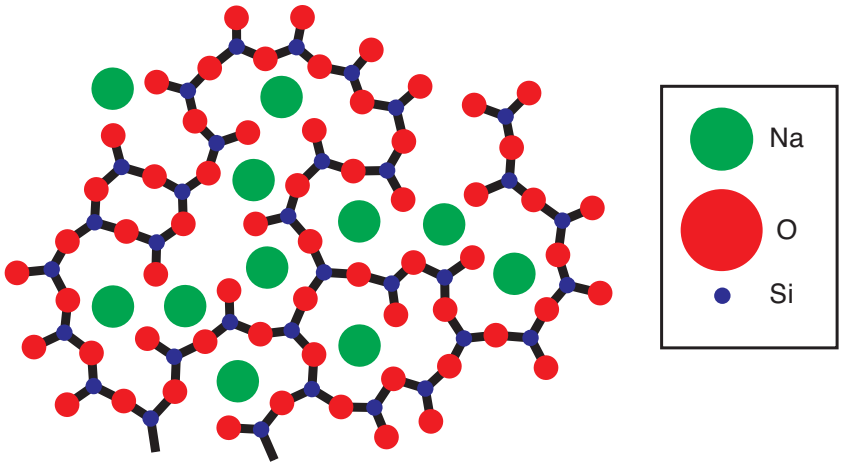

Figure 1.3: The random network model as proposed by Warren and Briscoe [3], where the network modifying cations cluster randomly throughout the glass structure.

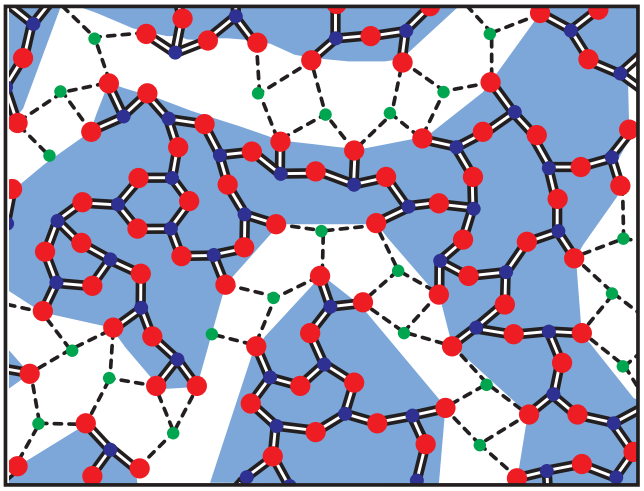

Figure 1.4: The modified random network model as proposed by Greaves [4] shows the network modifying cations (green) forming clustering channels within in the glass structure. While the silicon (blue) and oxygen (red) form a polymerized random network.

Greaves, in 1985, utilized extended X-ray absorption fine structure (EXAFS) to study the glass structure. Based on these results a modified random network model [4] was proposed by Greaves, where the network modifying cations are shown clustering in channels near the NBO sites, instead of randomly placed within the glass structure (Figure 1.4).

Understanding the local bonding environment around silicon can provide information on the structural disorder within the glass. The coordination of silicon is commonly denoted as $Q^{(n)}$ where n is the number of bridging oxygen per silicate tetrahedron and ranges from zero to four. The structure of glass, in contrast to crystals, is not dictated by the requirements of a fixed unit cell, prohibiting detailed analysis by diffraction based techniques.

One way to explore these structural models for the cation clustering in silicate glasses is by examining the thermodynamic disproportionation equilibria of the $Q^{(n)}$-species. The reaction,

$$2Q^{(n)} = Q^{(n+1)} + Q^{(n-1)},\ where\ n = 3, 2, 1, \tag{1.1}$$

represents this thermodynamic model. The concentrations of the $Q^{(n)}$-species are used to calculate the disproportionation constant, k_n, by the equation,

$$k_n = \frac{[Q^{(n+1)}][Q^{(n-1)}]}{[Q^{(n)}]^2}. \tag{1.2}$$

If a binary distribution of $Q^{(n)}$-species exists in the glass then all of the k values will be equal to zero. However, if $k_3 = 0.375$, $k_2 = 0.495$, and $k_1 = 0.311$ then the distribution of $Q^{(n)}$-species is considered to be random [42, 43]. A binary distribution of $Q^{(n)}$-species, as observed by Dupree et al. [44], has only two $Q^{(n)}$-species present at a time with sequential appearance of the next $Q^{(n)}$-species as the modifying cation concentration increases, as shown on the left of Figure 1.5. The random distribution model mentioned above any $Q^{(n)}$-species can exist at a given cation concentration, as shown on the right of Figure 1.5

1.1.4 Previous Structural Investigations of Silicate Glasses

Vibrational techniques, such as infrared transmission or reflection, or Raman scattering, have been extensively used for the investigation of the atomic-level structure of amorphous solids, specifically silicate glasses [45]. Raman scattering was instrumental in the early understanding of glass structure, especially in silicate glasses [13], including the observation of the dependence on composition of the polymerization state of silicate glasses [45]. Raman spectroscopy has been utilized to describe the short and

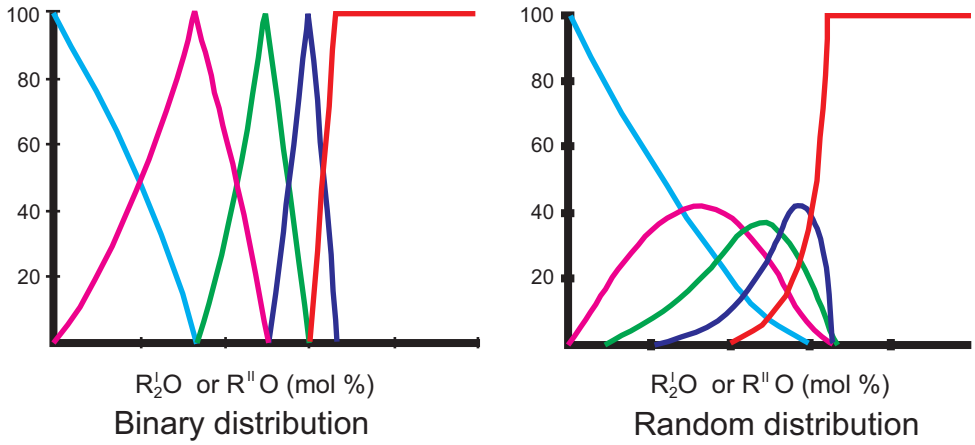

Figure 1.5: The thermodynamic model of a binary model (left) and a random model (right) for the $Q^{(n)}$-species distribution in silicate glasses containing varying concentrations of network modifying cations.

medium range bonding order in silicate glasses by identifying different $Q^{(n)}$-species within the glass [13, 46–49]. Raman studies also revealed that in silicate glasses with high alkali concentrations the silicate tetrahedra form 4-6 member rings [50]. The distinct difference between the silicon coordination environment in stishovite, which is known to have six coordinate silicon, and quartz that was observed by Lyon [51] was the first observation of the tetrahedral environment of silicon in quartz.

X-ray and neutron scattering and diffraction techniques have also been used to study the atomic-level structure of glasses [52]. Scattering and diffraction techniques yield results in terms of distances and angles within the structure of the molecule that is being studied, such as the radial distribution function ($T_x(r)$), shown in Figure 1.6, which is a measure of the density of atoms a distance, r, from the atom of interest [5]. Therefore, a distribution of interatomic distances and angles within the glass structure

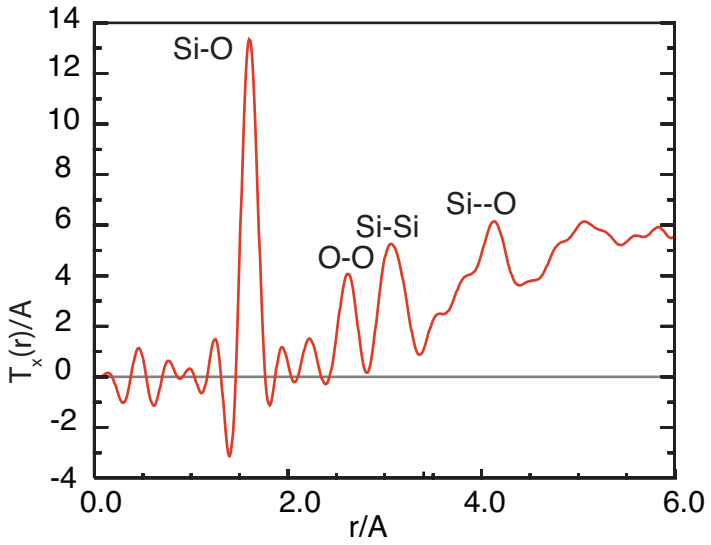

Figure 1.6: The radial distribution function ($T_x(r)$) of silica glass [5]. The radial distribution function is calculated by taking the Fourier transform of acquired diffraction data and is a measure of the density of atoms at distances, r, from the atom of interest.

can be obtained from X-ray and neutron scattering or diffraction studies of silicate glasses. Along with silicate glasses, structural details of germanium [53], titanium [54], and boron [55] oxide glasses have been studied using XRD and neutron diffraction experiments. X-ray absorption techniques, such as EXAFS, have also been routinely performed to study the structure of silicate glasses [52].

The first order coordination sphere that was described by Zachariasen [2] was confirmed using XRD, infrared spectroscopy, and neutron diffraction [3, 53, 55–59]. The radial distribution function of silica glass [5] indicates that there is a range of interatomic Si-Si distances (Figure 1.6), in agreement with the proposed structure by Zachariasen [2]. While these other spectroscopic techniques have been used to study the structure of silicate glasses, nuclear magnetic resonance (NMR) has proven

especially useful because of the ability to separate each $Q^{(n)}$-species through the resonance shift [7, 60–64]. NMR spectroscopy also allows for accurate quantification of the $Q^{(n)}$-species within the glass structure [6, 63, 64]. The relative abundance of each $Q^{(n)}$-species is determined by integrating the area under each resonance shift.

1.2 Nuclear Magnetic Resonance

Discovered in 1945, NMR spectroscopy is a technique that detects the nuclear spin of molecules precessing in a magnetic field. NMR spectroscopy can be used to identify nuclei with different bonding environments within a particular molecule, due to differing resonance shifts.

1.2.1 Macroscopic Model of NMR Active Nuclei

Thinking of a nuclear spin as a macroscopic spinning top is a useful macroscopic model for NMR. If the spinning top is placed in a zero gravity environment the top will not precess. However, if the top is then placed in a gravitational field, Figure 1.7A, then the top will precess about the direction of the gravitational field, with a characteristic frequency that is determined by parameters that are unique to the particular top and environment, such as the mass and moment of inertia of the top, and the gravitational field strength. If a bar magnet is placed along the spinning axis of the top, and the top is placed within a magnetic field the top will begin precessing about the magnetic field axis (Figure 1.7B). The top will precess with a characteristic frequency, ω_0, called the Larmor frequency. The Larmor frequency is linearly related to the strength of the external magnetic field, B_0. By wrapping a wire, or coil, around the precessing top, as shown Figure 1.8, Faraday's Law can be

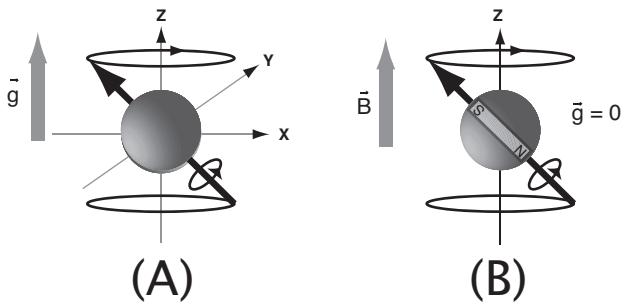

Figure 1.7: A macroscopic spinning top (A) placed in a gravitational field precessing about the direction of the gravitational field (along the z axis). A spinning top with a bar magnet inside (B) placed in a magnetic field (along the z axis) precessing about the external magnetic field, B_0.

exploited to measure the change in magnetic flux,

$$\mathcal{E} = -\frac{d\Phi}{dt}, \tag{1.3}$$

where $\mathcal{E}$ is the Electromotive Force, EMF, and Φ is the magnetic flux. The EMF, $\mathcal{E}$, that is induced in the coil is given by

$$\mathcal{E}_x(t) = \omega_0 \frac{\mu_0}{2r_{coil}} |\mu| \sin\psi \sin(\omega_0 t + \xi_0), \tag{1.4}$$

where ω_0 is the precession frequency, $|\mu|$ is the length of the precessing magnetization vector, ψ is the angle between the z axis and the precessing magnetization vector, and ξ_0 is the initial phase of the vector, as shown in Figure 1.9. The amplitude of the signal that is acquired is proportional to the magnetic dipole strength and the angle from the external magnetic field axis. The Electromotive force is maximized when the angle ψ is perpendicular to the external magnetic field axis.

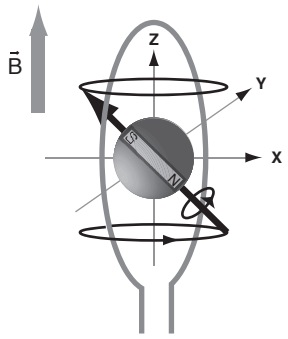

Figure 1.8: The spinning magnetic top precessing about the external magnetic field, B_0 will induce an EMF, $\mathcal{E}$, in the coil wrapped parallel to the external magnetic field direction.

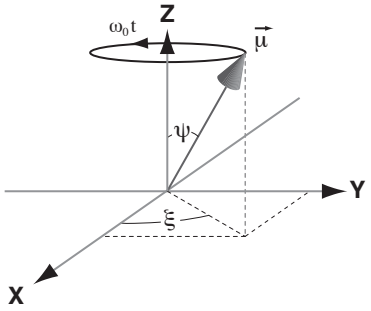

Figure 1.9: The magnetization vector $\vec{\mu}$ as it precesses about B_0, shown in the cartesian coordinate system.

1.2.2 Magnetic Resonance

Each NMR active nucleus (one that has spin angular momentum that is not equal to zero) can be thought of as a microscopic spinning top. When an NMR active nucleus is placed into a magnetic field then the coupling between the magnetic dipole vector and the external magnetic field will cause the nucleus to precess about the external magnetic field axis. The Larmor frequency that a nucleus precesses at is determined, to first order, by the gyromagnetic ratio, γ, and the magnetic field strength, B_0, by the equation,

$$\omega_0 = -\gamma B_0. \tag{1.5}$$

The nuclear gyromagnetic ratio is dependent on the nucleus. The Larmor frequency of a nucleus is caused by the coupling between the magnetic dipole vector of the nucleus and the external magnetic field, called the Zeeman interaction. As discussed in the section above, the amplitude of the NMR signal is proportional to the angle the net magnetization vector is from the external magnetic field. Therefore, to detect the maximum signal the bulk magnetization of the sample must be in the xy plane. However, the bulk magnetization in an external magnetic field will be aligned along the direction of B_0. The bulk magnetization is placed in the xy plane by applying a small secondary magnetic field, B_1, in the form of a radio frequency (rf) pulse into the coil, which serves to tilt the net magnetization from the z axis. This B_1 field is applied multiple times until the net magnetization is in the xy plane. The magnetic resonance phenomenon is shown in Figures 1.10 and 1.11.

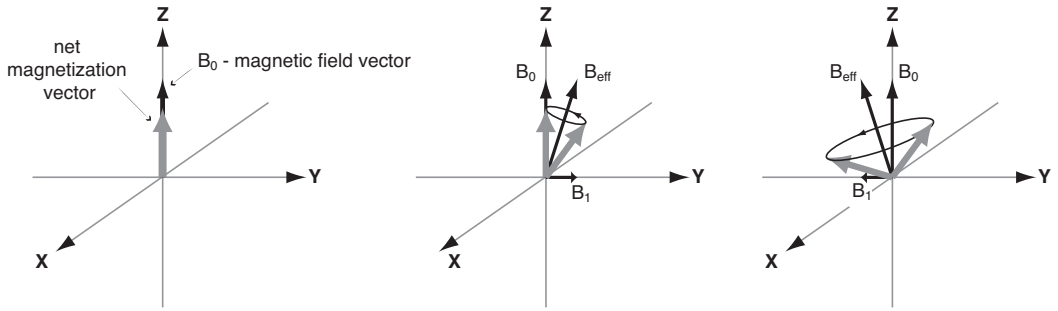

Figure 1.10: The net magnetization aligns along the external magnetic field direction, B_0. A small magnetic field B_1 is applied in the form of an rf pulse along the $+y$ axis. The net magnetization then tips slightly toward the $+y$ axis from the $+z$ axis. Once a precession of 180° is achieved another B_1 magnetic field is applied along the $-y$ axis, which causes the magentization to tilt further from B_0.

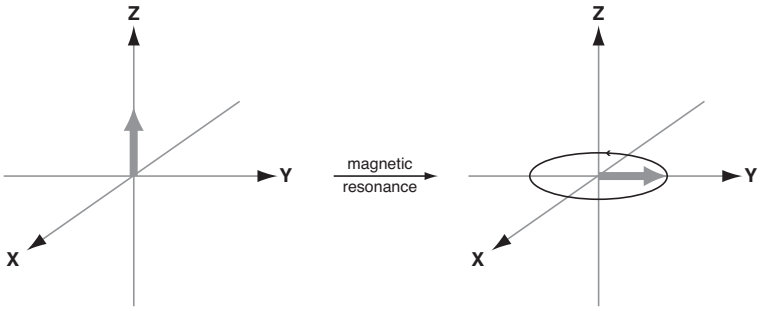

Figure 1.11: The result of magnetic resonance is shown, where the alternating small magnetic fields shown above have shifted the net magnetization vector from the $+z$ axis into the xy plane.

1.2.3 Nuclear Shielding and Chemical Shift

The varying resonance shifts in a sample are caused in part by the nuclear shielding of the NMR active nucleus, where the nuclear shielding of a particular NMR nucleus in a fixed molecule system is defined by the second rank tensor (note that bold face text will be used to denote a variable that is a tensor),

$$\boldsymbol{\sigma} = \begin{pmatrix} \sigma_{xx} & \sigma_{yx} & \sigma_{zx} \\ \sigma_{xy} & \sigma_{yy} & \sigma_{zy} \\ \sigma_{xz} & \sigma_{yz} & \sigma_{zz} \end{pmatrix} \tag{1.6}$$

Each unique bonding environment around the NMR active nucleus yields a different resonance shift. Based on the geometry of the molecule, local magnetic fields are induced in the molecule that increase, or decrease, the net magnetic field that is experienced by the nucleus with respect to the shielding of a reference compound [65]. This increasing, or decreasing, of the net magnetic field is called nuclear shielding, or deshielding, where the nuclear shielding value for a particular NMR nucleus is given with respect to a bare nucleus, where $\boldsymbol{\sigma} = 0$. Therefore, all nuclear shielding values are positive, and increasing nuclear shielding values correspond to a larger density of electrons near the nucleus. The nuclear shielding of the NMR center causes the unique resonance frequency that is characteristic of an NMR spectrum. Therefore, the geometry of molecules can be explored by determining the nuclear shielding of each unique site. The nuclear shielding effect is accounted for in the precession frequency, ω, by the equation

$$\omega = -\gamma(1 - \sigma_{iso})B_0, \tag{1.7}$$

where σ_{iso} is the isotropic nuclear shielding. The isotropic nuclear shielding is defined as

$$\sigma_{iso} = \frac{1}{3}Tr\left\{\boldsymbol{\sigma}\right\} = \frac{1}{3}(\sigma_{zz} + \sigma_{yy} + \sigma_{zz}), \tag{1.8}$$

where the trace of the second rank nuclear shielding tensor is the components, or eigenvalues, of the tensor in its principal axis system. The nuclear shielding tensor is important because it describes the shielding interaction in three-dimensional space. The nuclear shielding tensor can be thought of as an ellipsoid in three-dimensional space; however, this is best understood if the isotropic nuclear shielding is subtracted from the diagonal components of the nuclear shielding tensor yielding,

$$\lambda_{zz} = \sigma_{zz} - \sigma_{iso}, \tag{1.9}$$

$$\lambda_{yy} = \sigma_{yy} - \sigma_{iso}, \tag{1.10}$$

$$\lambda_{xx} = \sigma_{xx} - \sigma_{iso}. \tag{1.11}$$

In this reference frame the λ values describe deviations, positive or negative, from a sphere. The direction of the deviation in three-dimensional space is determined by the eigenvector of the particular component of the nuclear shielding tensor. While the nuclear shielding tensor is asymmetric it is treated as symmetric ($\sigma_{xy} = \sigma_{yx}$) as a first-order approximation [66]. It is difficult to determine the nuclear shielding of the nucleus of interest due to the fact that a precise measurement of the B_0 field is required, which means the magnetic susceptibility of the sample must be taken into account. Therefore, chemical shift is often used to label resonance shifts due to its convenience. A chemical shift value (δ_{ij}) can be calculated for each of the nuclear shielding tensor components creating a chemical shift tensor. The isotropic chemical shift of a sample is defined as,

$$\delta_{iso} = \frac{\omega_{iso} - \omega_{ref}}{\omega_{ref}} \tag{1.12}$$

in terms of the NMR frequency, and

$$\delta_{iso} = \frac{\sigma_{ref} - \sigma_{iso}}{1 - \sigma_{ref}} \tag{1.13}$$

in terms of the nuclear shielding of the molecule, where σ_{ref} and ω_{ref} are the nuclear shielding and the NMR frequency, respectively, of a reference compound. Therefore, the chemical shift values have the opposite sign as nuclear shielding and as the nucleus becomes more shielded the chemical shift value decreases. The chemical shift trends that are obtained from an NMR experiment can be related to the nuclear shielding trends, which in turn are related to the electron density around the nucleus. However, relating the chemical shifts values to nuclear shielding values is difficult due to the fact that an exact nuclear shielding reference is required.

In powdered samples, the NMR frequency contains contributions from each unique orientation of the crystallite with respect to the external magnetic field. While this causes NMR lineshapes to become significantly broadened because of the underlying anisotropy, analyses of these lineshapes can provide rich structural detail around nuclei of interest. The primary interaction for spin I = $\frac{1}{2}$ nuclei, like ^{29}Si, is the nuclear shielding which gives rise to an anisotropic lineshape. Stebbins [6] realized that each $Q^{(n)}$-species has a distinct anisotropic lineshape (Figure 1.12), and used this relationship to separate multiple sites in the static ^{29}Si NMR spectra of glasses. Therefore, the anisotropic lineshapes of silicate glasses can be used to identify the $Q^{(n)}$-species. The distinct anisotropic lineshapes of the $Q^{(n)}$-species can be related to the nuclear shielding based on the effect each nuclear shielding eigenvalue has on the lineshape, as shown in Figure 1.13. When using the Haeberlen convention [67],

$$|\sigma_{zz} - \sigma_{iso}| > |\sigma_{yy} - \sigma_{iso}| > |\sigma_{xx} - \sigma_{iso}|, \tag{1.14}$$

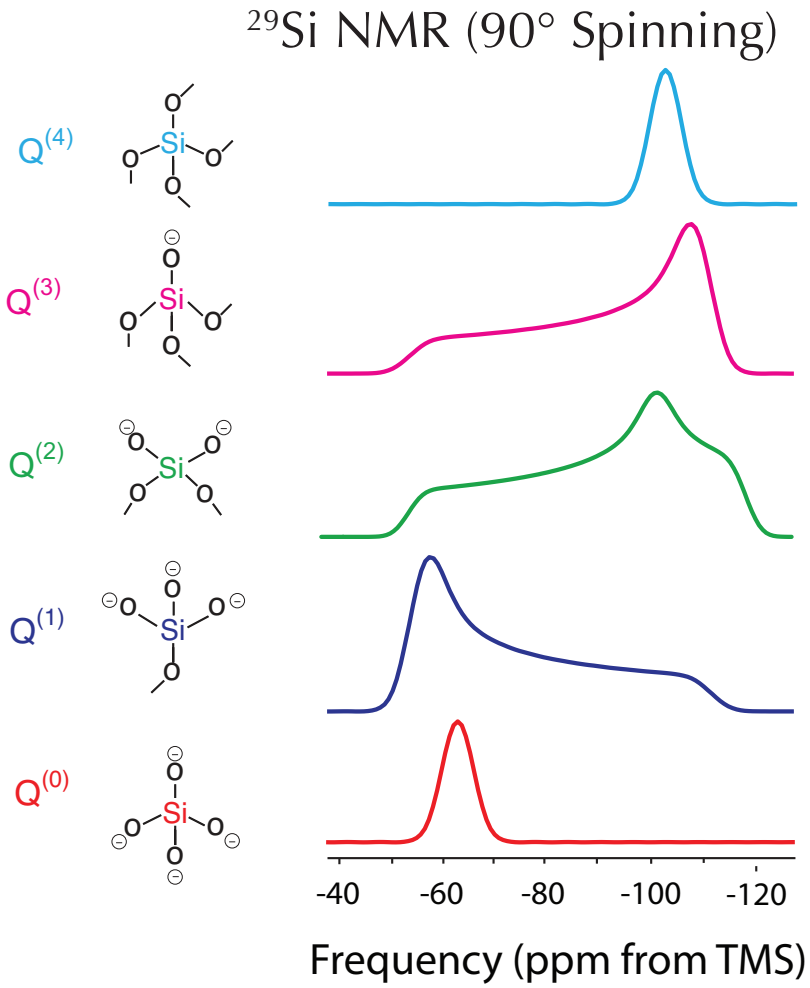

Figure 1.12: The distinct anisotropic lineshape of each $Q^{(n)}$-species for ^{29}Si NMR (shown as spinning at 90° with respect to the magnetic field) as shown by Stebbins [6].

the anisotropy of the NMR lineshape can be described by using two parameters, ζ and η, which are defined as,

$$\zeta_\sigma = \sigma_{zz} - \sigma_{iso},\ or\ \zeta_\delta = \delta_{zz} - \delta_{iso}, \tag{1.15}$$

and

$$\eta = \frac{\sigma_{yy} - \sigma_{xx}}{\sigma_{zz} - \sigma_{iso}} = \frac{\sigma_{yy} - \sigma_{xx}}{\zeta_\sigma},\ or\ \eta = \frac{\delta_{yy} - \delta_{xx}}{\zeta_\delta} \tag{1.16}$$

where ζ_σ is the nuclear shielding anisotropy, ζ_δ is the chemical shift anisotropy, and η is the nuclear shielding asymmetry parameter of the nuclear shielding tensor. ζ and η describe the shape, deviation from spherical, of the nuclear shielding tensor. Therefore a nuclear shielding tensor where both ζ and η are zero is a sphere in three-dimensional space. As the symmetry of the electron density around the nuclei of interest decreases the magnitude of the anisotropy, ζ, increases. However, η increases when the asymmetry of the nuclear shielding tensor becomes increasingly multi-directional. This asymmetry in the nuclear shielding tensor arises due to the Si-NBO bonds of the $Q^{(n)}$-species and the cation clustering around each non-bridging oxygen. This allows each $Q^{(n)}$-species to be resolved due to the anisotropic lineshape and unique chemical shift value.

1.2.4 Magic Angle Spinning

Magic angle spinning [68–70] reorients the sample to average away the anisotropy in powdered solids by simulating the continuous reorientation of liquid state NMR by spinning the sample, packed in a rotor, rapidly about a fixed angle. The magnitude of the anisotropy scales as the second-order Legendre polynomial, $P_2cos(\theta)$, which is zero when the angle, θ, is 54.74°, which is called the magic angle. The magic angle

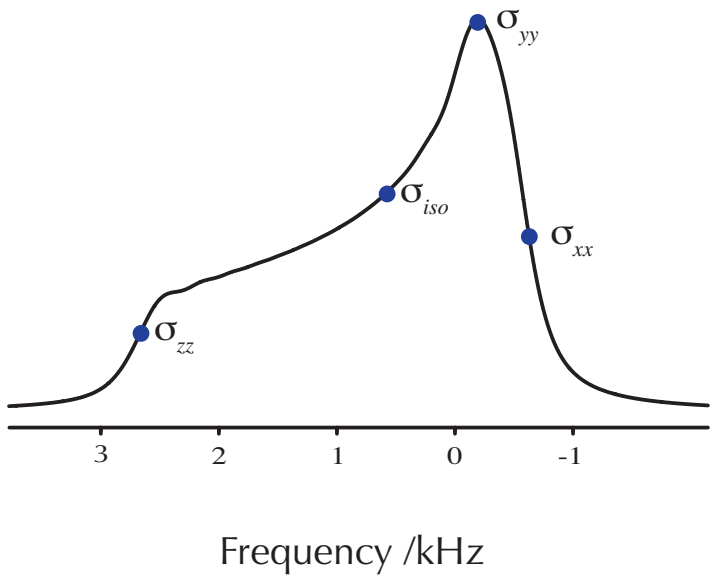

Figure 1.13: The contributions of the nuclear shielding tensor parameters on the anisotropic lineshape.

is typically chosen due to the fact that while spinning at the magic angle the second-order anisotropic interactions are averaged to zero assuming that the spinning speed is greater than the width of the anisotropy. Spinning sidebands appear at integer multiples of the spinning speed if the spinning speed is not sufficiently fast enough (Figure 1.14). Averaging away the anisotropy of the NMR lineshape increases the sensitivity of the spectrum because the total integrated area of the broad powder pattern has been collapsed into a narrow resonance with MAS.

The chemical shift values for each $Q^{(n)}$-species within silicate glasses are well known [71–73]. While MAS is effective, the MAS lineshapes in glasses are composed of a distribution of isotropic chemical shifts that lead to broad overlap in the NMR spectrum, due to the disordered nature of glass resonance. These broad overlaps in

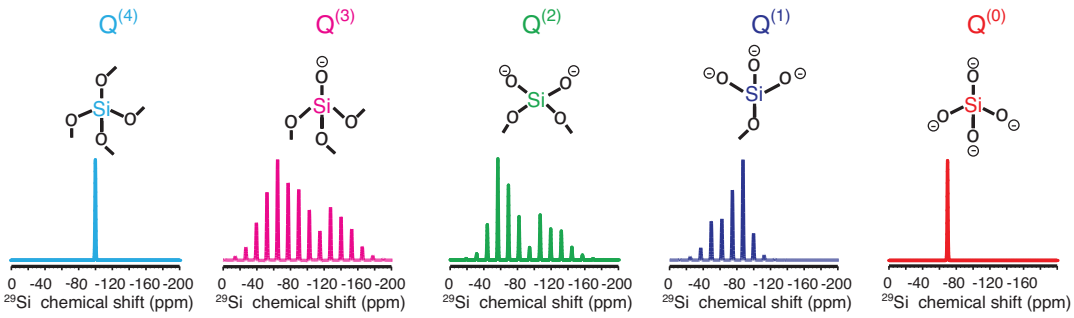

Figure 1.14: The characteristic spinning sideband pattern of each $Q^{(n)}$ species when the spinning speed is less than the width of the anisotropy for the sample.

the MAS NMR spectrum lead to broad Gaussian lineshapes [74]. In order to improve resolution various multidimensional NMR techniques have been developed to correlate a pure isotropic dimension, which contains narrower, albeit overlapping, NMR lineshapes, to a purely anisotropic dimension where broad anisotropic lineshapes are observed [75–78]. The benefit of this approach is that narrow lineshapes can be acquired while maintaining the structural information contained within the anisotropic powder patterns. The two-dimensional experiments that can be used to correlate purely anisotropic and a pure isotropic dimension include Magic Angle Hopping (MAH) [75], Magic Angle Flipping (MAF) [75], Magic Angle Turning (MAT) [76], and 2D Phase Adjusted Spinning Sidebands (2D PASS) [77, 78].

1.2.5 Magic Angle Flipping

The 2D MAF experiment reorients the rotor axis between two angles, typically magic (54.74°) and 90° with respect to the magnetic field, to manipulate the spatial dependence of the chemical shift anisotropy. The magnetization is allowed to evolve for a variable time, t_1, while spinning at 90° with respect to the magnetic field. The

variable time, t_1, makes MAF a two-dimensional experiment. Because the magnitude of the anisotropy scales as the second-order Legendre polynomial, $P_2cos(\theta)$, when the rotor is spinning at 90° with respect to the external magnetic field the anisotropy is introduced because $P_2cos(\theta) = -0.5$ [79]. Following the evolution period the magnetization is stored and the rotor is mechanically hopped, using a stepper motor, to the magic angle where the anisotropy is fully averaged away. The signal can then be detected, or the echo can be shifted out in time to ensure the entire echo is collected [75,80]. The resulting 2D data is amplitude modulated in t_1 by the contribution of the anisotropy. A 2D frequency domain spectrum that correlates a dimension that is a 90° dimension and the MAS dimension is produced by a 2D Fourier transform. The 90° dimension can be transformed into a purely anisotropic dimension through a shear of the 2D data. The data can then be fit using the unique isotropic chemical shift values for each $Q^{(n)}$ site. The MAF experiment is limited due to the need for specialized hardware and the fact that it causes broadening in the MAS dimension. Carr-Purcell-Meiboom-Gill (CPMG) echo train acquisition [81,82] can be used to enhance the sensitivity of the 2D MAF experiment. In the experiments that follow the angle pair has been switched; therefore, the anisotropic contributions evolve during the echo shift, τ_{echo}, and the isotropic contribution evolves during t_1. This effectively exchanges the broad and narrow dimensions.

1.3 *Ab Initio* Calculations of the Nuclear Shielding Tensor

Computational chemistry has proven itself a powerful tool when used to correlate experimental and theoretical trends [83–90]. The use of *ab initio* quantum chemical calculations to model large clusters has become more practical with advances in

computing power. *Ab initio* quantum chemical calculations use linear combinations of functions, typically Gaussian functions, to approximate the wave function of the molecule. The approximate wave function is then utilized to calculate the parameters that are desired using the fundamental laws of quantum mechanics. Computational chemistry can be used to calculate the NMR parameters for small molecules and clusters that mimic the short-range structure of larger molecules. Cheeseman et al. [91] explored the level of theory and basis set that can most accurately calculate the nuclear shielding tensor, with respect to computational cost, of certain NMR active nuclei using various cluster sizes. Using *ab initio* quantum chemical calculations to correlate theoretical trends to experimental results can help elucidate structural details of amorphous materials.

The nuclear magnetic shielding tensor is calculated in *ab initio* calculations as a perturbation of the overall Hamiltonian and is expressed as the mixed second derivative of the energy [91],

$$\sigma_{ji}^{N} = \frac{\partial^2 E}{\partial B_i \partial m_{N_j}}, \tag{1.17}$$

where i and j are the components of the external magnetic field and the induced magnetic moment respectively. This is used by computational software packages to calculate the nuclear magnetic shielding tensor of each nucleus in the molecule. There are several different methods that are available for calculating the nuclear shielding tensor, including gauge-independent atomic orbital (GIAO), and continuous set of gauge transformations (CSGT). These methods differ in how the nuclear shielding tensor is calculated within the overall Hamiltonian function during the *ab initio* quantum chemical calculations and have been extensively studied [91].

The next chapter will focus on the use of *ab initio* calculations to confirm experimental trends found in network modified silicate glasses. Combining the theoretical trends obtained from *ab initio* quantum chemical calculations with experimental trends can be useful to provide confirmation of the experimental model being presented.

The third chapter will focus on the use of 2D MAF NMR to study the clustering of network modifying cations in a mixed potassium/magnesium tetra-silicate glass. The clustering of the network modifying cations can provide insight into the long-range structural order of mixed modified glasses.

CHAPTER 2

Computational Investigation of ^{29}Si Nuclear Shielding Tensors in Network-Modified Silicate Glasses

2.1 Introduction

Previous studies have been conducted by Grandinetti and Clark [89, 90] using *ab initio* quantum calculations to correlate ^{17}O quadrupolar coupling parameters to the Si-O bond distance and Si-O-Si bond angle in silicate glasses. The correlation between the ^{29}Si nuclear shielding tensor parameters and Si-O bond distance can be achieved by using computational chemistry. *Ab initio* quantum chemical calculations can be used to calculate the nuclear shielding tensor and output its cartesian coordinates for tetrahedral silicate clusters emulating $Q^{(n)}$-species with varying bond distances to simulate different cation clustering environments within the glass structure. The nuclear shielding tensor of the silicon center changes with changes in the bonding environment near the ^{29}Si nucleus [9]. This can be shown through changes in either the nuclear shielding anisotropy or the nuclear shielding asymmetry parameter. The nuclear shielding anisotropy can be calculated from the nuclear shielding tensor for each $Q^{(n)}$-species and used to correlate the experimental results for the $Q^{(n)}$-species within the glass structure to bonding environment of each non-bridging oxygen within the glass structure. Grimmer and coworkers [9, 10] reported experimentally obtained

trends correlating Si-NBO bond distance with a nuclear shielding tensor eigenvalues. Davis et al. [7, 8] determined experimentally that there was a strong correlation between increasing cation potential of the modifying cation and decreasing magnitude of the chemical shift anisotropy. This trend was related to the previous trend reported by Grimmer, and it was determined that as cations with higher cation potential are incorporated into the glass, the Si-NBO bond length must be decreasing. Thus, it is important to combine theoretical trends correlating the magnitude of the anisotropy to a change in Si-NBO bond distance to confirm the experimental trends reported in previous studies. Therefore, in this study we will correlate the changes in the nuclear shielding tensor with changing ^{29}Si bonding environment to the experimentally observed trends in the chemical shift anisotropy.

2.2 Computational Methods

The nuclear shielding tensors were investigated using *Gaussian 03* [92] at a Hartree-Fock level with a 6-311+G(2d,p) basis set used for all atoms. The nuclear shielding tensor elements for the molecule of interest, a silicate tetrahedron with varying Si-NBO bond distance that was built to model different $Q^{(n)}$-species with various modifier cations, were calculated using *Gaussian 03*. Calculations were performed on silicon centered clusters, as shown in Figure 2.1, that were built in the axis system shown to the right of each cluster (the axis not shown in both A and B of Figure 2.1 is positive coming out of the page). These clusters were built in their principal axis system with respect to the perturbation of the Si-O bond distances that was to be performed. These clusters were built in a $Q^{(4)}$ environment, using a Si-O bond distance of 1.61 Å based on the bond distance of α-quartz [10, 93], with hydrogens bonded to

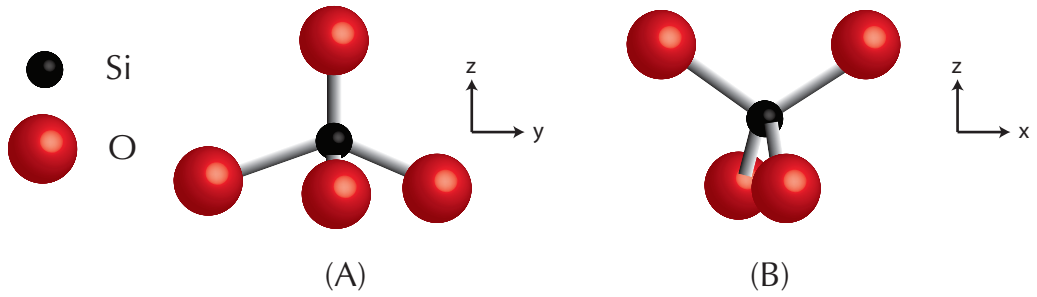

Figure 2.1: Silicon centered clusters that were built in their principal axis system, shown to the right of each cluster, with respect to the perturbation dependent on the $Q^{(n)}$-species that was being modeled. The axis that is not shown in positive coming out of the page. (A) the $Q^{(3)}$ and $Q^{(1)}$ cluster is shown, and (B) the $Q^{(2)}$ cluster is shown.

the end of each oxygen anion and held at a bond angle of 180° (not shown). These clusters were built to emulate the first coordination sphere of a silicate tetrahedron of various $Q^{(n)}$-species. The $Q^{(3)}$ clustering environment was made from the cluster shown in Figure 2.1A by decreasing the Si-O bond, by 0.01 Å from 1.61 Å to 1.51 Å, that is at the top of the cluster. This depression of the Si-O bond distance simulates the changing Si-NBO bond distance in the presence of different network modifying cation. The $Q^{(2)}$-like cluster was made by decreasing the Si-O bond distance of two bonds at the top of the cluster shown in Figure 2.1B to 1.51 Å in steps of 0.01 Å. The $Q^{(2)}$ clusters were simulated by a symmetric depression of the two Si-NBO bonds, which is meant to model a $Q^{(2)}$ site with a single modifying cation. The $Q^{(1)}$ cluster was built using the same starting cluster as the $Q^{(3)}$ cluster; however, the Si-O bond was stretched to 1.71 Å, by 0.01 Å, to simulate the other three oxygens as non-bridging oxygens and the perturbed oxygen as the bridging oxygen. This difference in the bond that is being changed has no effect on how the tensor changes

based on the change in bonding environment near the ^{29}Si nucleus. The changing Si-O bond distance should in theory be placing more or less electron density near the ^{29}Si nucleus.

2.3 Results and Discussion

The nuclear shielding tensor parameters for the $Q^{(3)}$ like cluster, shown on the left side of Figure 2.2, were determined to become more shielded along the z axis, while becoming deshielded along the x and y axes as the Si-NBO bond distance was decreased from the $Q^{(4)}$ α-quartz parameters. The λ_{zz} value is also the nuclear shielding anisotropy for the cluster. Therefore, the magnitude of the anisotropy, ζ, for the $Q^{(3)}$ cluster was determined to become greater as the Si-NBO bond distance decreased in agreement with the previously reported trend by Grimmer and coworkers [9, 10]. Thus, as the Si-NBO bond distance increases the electron density near the silicon nucleus decreases causing the z axis to be deshielded. This is found to be in agreement with the correlation found by Davis et al. [7, 8] that as cations with higher cation potential are incorporated into the glass structure the Si-NBO bond distance increases causing the chemical shift anisotropy to decrease. This decrease in ζ corresponds to the nuclear shielding tensor becoming more symmetric due to the Si-NBO bond distance approaching the distance of the Si-BO bond distance. The cluster that is shown in the center of Figure 2.2, and on the right of Figure 2.3, represents the symmetric $Q^{(4)}$ environment and is shown with a spherical nuclear shielding tensor, represented by all zero λ values. The cluster that is shown in the top left corner of Figure 2.2 represents a $Q^{(3)}$ cluster that is modified by a weak cation, due to the short bond (1.51 Å). Based on the trends in the principal components of the nuclear

shielding tensors the shape of the nuclear shielding tensor changes from a football along the z axis to a sphere as the cation potential of the network modifying cation are increased.

The $Q^{(1)}$ cluster calculations determined that the ^{29}Si nucleus became deshielded along the z axis, while along the x and y axes the ^{29}Si nucleus became more shielded as the Si-NBO bonds were effectively decreased, as shown on the right side of Figure 2.2. The magnitude of the nuclear shielding anisotropy, shown as λ_{zz} in Figure 2.2, of the $Q^{(1)}$ cluster was found to increase with decreasing Si-NBO bond distance, in agreement with the previous results [7–10]. Due to the fact that the far right of the graph represents the shortest Si-NBO bonds, the cluster in the top right corner of Figure 2.2 is a representation of what the bonding environment of a silicate tetrahedron might be like in the presence of a weak network modifying cation. For this type of cluster the nuclear shielding tensor has effectively been perturbed from a sphere into a pancake-like shape in the xy plane. Therefore, as the cation potential of the network modifying cation in a $Q^{(2)}$ site is increased the nuclear tensor transforms from this shape into a sphere.

The $Q^{(2)}$ site cluster with a single network modifying cation was determined to become more deshielded along the y axis, which is orthogonal to the Si-NBO bods, while becoming more shielded along the x axis, which is parallel to the Si-NBO bonds, based on the principal nuclear shielding tensor components (Figure 2.3). The z axis, which is between the two Si-NBO bonds, remained unchanged with respect to the perturbation. The changing nuclear shielding anisotropy is λ_{xx} as shown in Figure 2.3 due to the fact that the Haeberlen convention has been ignored to keep the molecule in the axis system in which it was built. Therefore, the nuclear shielding elements are

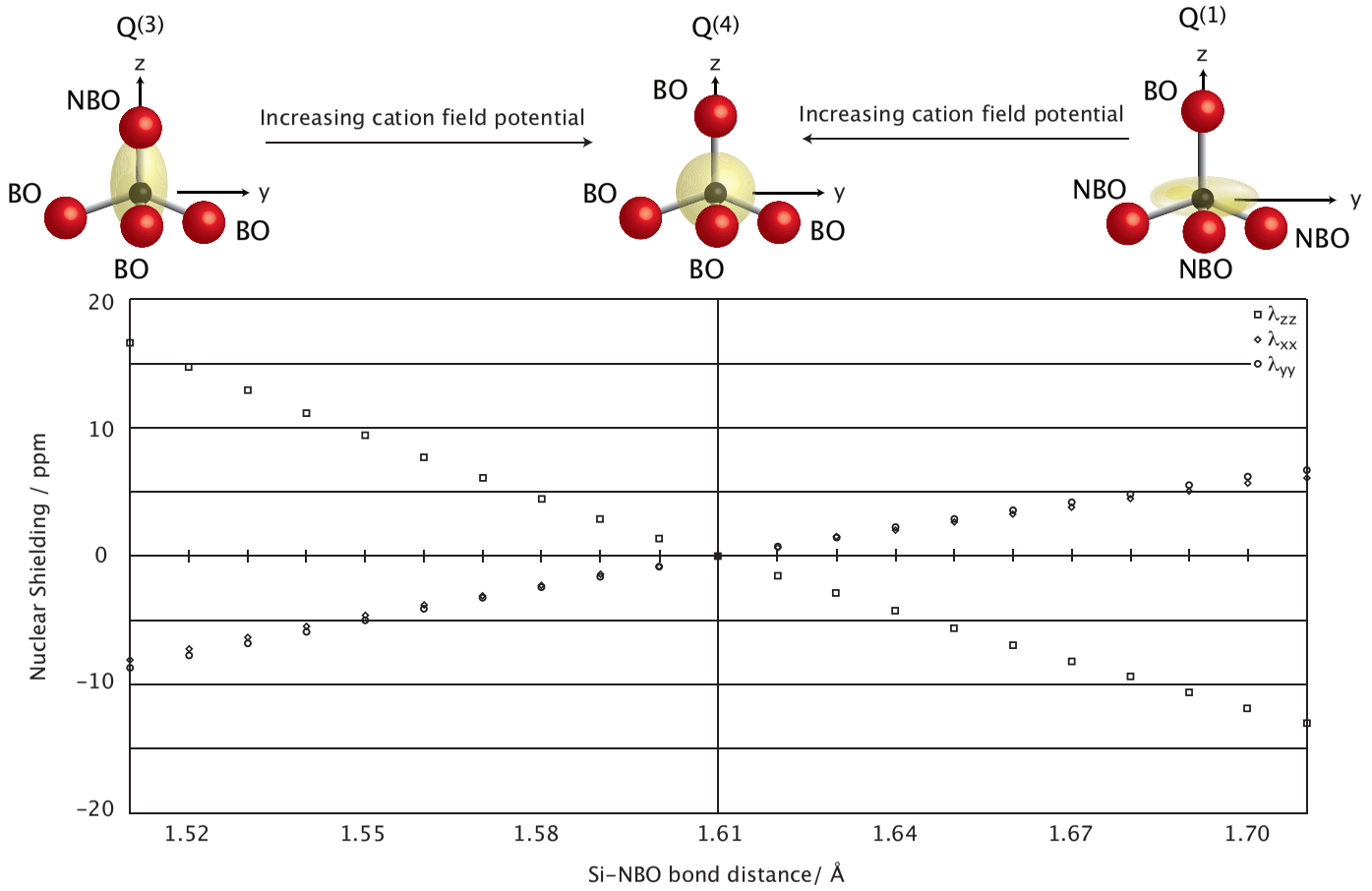

Figure 2.2: The *ab initio* computational results for the $Q^{(3)}$ (left side) and $Q^{(1}$ (right side) clusters for various Si-NBO bond distances. The Haeberlen convention has not been followed for the λ values shown and therefore the λ values correspond to their axis in the original (built) axis system. The nuclear shielding anisotropy for this axis system is defined as λ_{zz} and therefore is shown to be in agreement with the previous results [7–10]. The symmetric $Q^{(4)}$ cluster is shown in the middle above the graph with a spherical nuclear shielding tensor surrounding the ^{29}Si nucleus. The $Q^{(3)}$ cluster with a modifying cation (with a Si-NBO distance of 1.51 Å) is shown (top left) with a football-like tensor surrounding the ^{29}Si center. The cluster shown at the top right of the graph represents a $Q^{(1)}$ site with a Si-NBO bond distance of 1.51 Å for the and is shown with a pancake-like tensor surrounding the silicon nucleus. The tensor representations shown in this figure are based on the nuclear shielding tensor components. Note that the cation potential of the effective modifier cation increases towards the center of the graph.

along the axis in the original axis system as indicated in Figure 2.1B. The trend in changing anisotropy, as shown in Figure 2.3, with respect to Si-NBO bond distance was found to be in agreement with the previously reported trends [9, 10]. The tensor for a cluster emulating a weak network modifying cation is shown in the top left corner of Figure 2.3. Based on the trends in the nuclear shielding tensor components it has been determined that the shape of the nuclear shielding tensor transforms from a football in the xz plane that has been squeezed along y axis to a sphere as the cation potential of the network modifying cation increases.

The theoretical results obtained using *ab initio* quantum chemical calculations were found to be in good agreement with the previous experimental results [7–10] that were obtained using NMR spectroscopy. Therefore, the theoretical and experimental trends both indicate that the introduction of a network modifying cation with a greater cation potential yields an increase in the magnitude of the anisotropy due to the lengthening of the Si-NBO bond. This lengthening of the Si-NBO bonds causes a decrease in electron density near the ^{29}Si center along this bond.

2.4 Conclusions

The theoretical results obtained using *ab initio* quantum chemical calculations were found to be in good agreement with the previous experimental results [7–10] that were obtained using NMR spectroscopy. Therefore, the theoretical and experimental trends both indicate that the introduction of a network modifying cation with a greater cation potential yields an increase in the magnitude of the anisotropy due to the lengthening of the Si-NBO bond. This lengthening of the Si-NBO bond causes a decrease in electron density near the ^{29}Si center along this bond. This decrease in

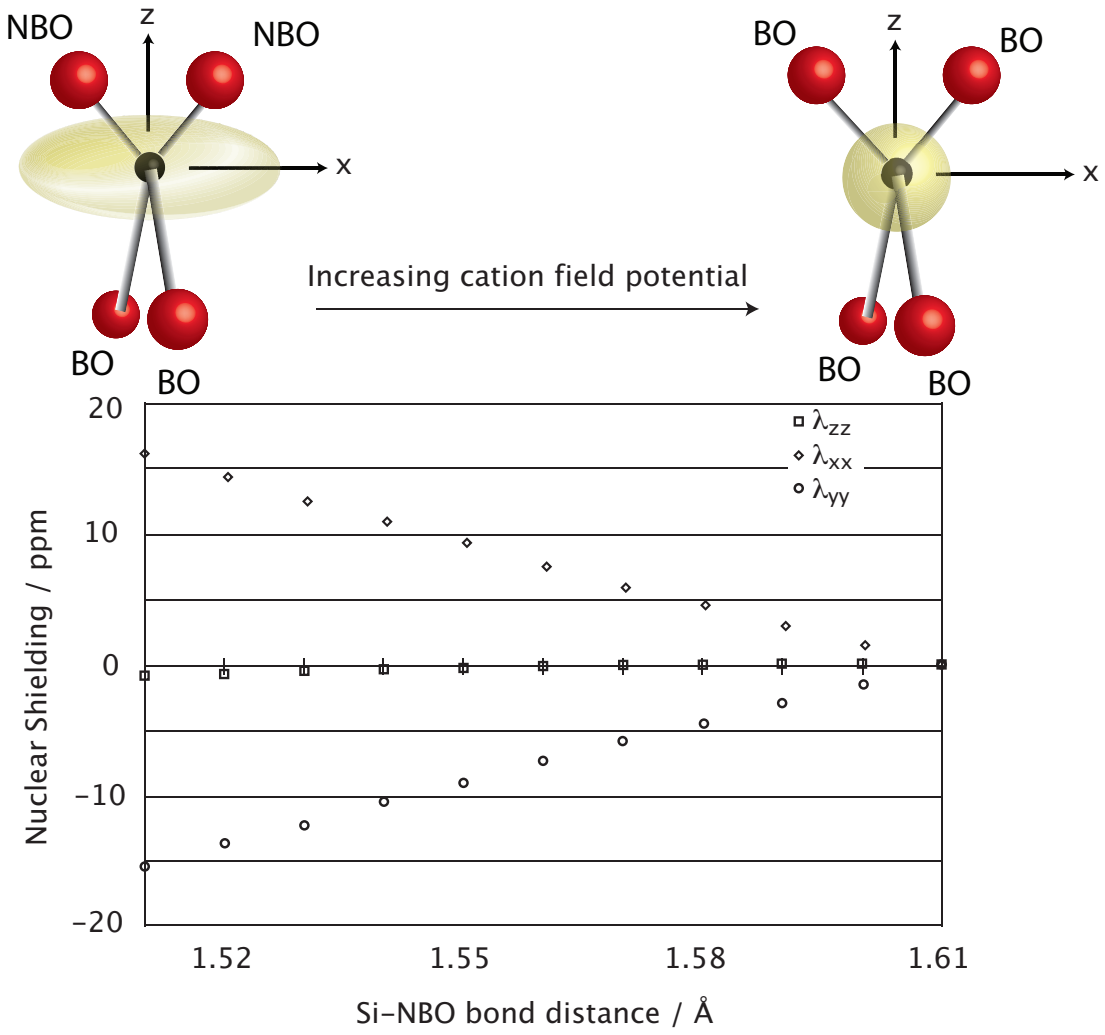

Figure 2.3: The *ab initio* results for the $Q^{(2)}$ cluster for Si-NBO bond distances between 1.61 Å and 1.51Å. The Haeberlen convention has been neglected for these results. Therefore, the λ values are along the respective direction from the original axis system. The nuclear shielding anisotropy for this axis system is defined as λ_{xx} and therefore is shown to be in agreement with the previous results [7–10]. The symmetric $Q^{(4)}$ cluster is shown to the top right of the graph with a spherical nuclear shielding tensor surrounding the silicon. The $Q^{(2)}$ cluster to the top left of the graph is shown for Si-NBO bond distance of 1.51 Å with the squeezed football shaped tensor surrounding the ^{29}Si nucleus. This tensor representation is based on the nuclear shielding tensor components.

electron density near the ^{29}Si center causes a decrease in shielding along the direction of decreasing electron density. Thus, network modifying cations with greater cation potential will cause an increase in the Si-NBO bond distance causing a decrease in the electron density in that direction around the ^{29}Si nucleus causing the change in the nuclear shielding tensor.

CHAPTER 3

$Q^{(3)}$-site Variations in a Mixed Potassium/Magnesium Glass using Natural Abundance ^{29}Si Magic Angle Flipping (MAF) NMR

3.1 Introduction

Previous studies by Greaves et al. [94, 95] using X-ray absorption fine structure (EXAFS) determined that the network modifying cations are regularly coordinated to the NBO sites in silicate glasses. Neutron diffraction studies [96, 97] have shown that the ordering of network modifying cations extends beyond the local bonding environment into the intermediate bonding environment by the determination of strong correlations between Ca-Ca and Ca-O distances in $CaSiO_3$ glasses. Nuclear magnetic resonance (NMR) has been routinely used to study the order, or disorder, of network modifying cations within the structure of glasses with only a single network modifying cation [1, 7, 8, 44, 60, 61, 98, 99]. However, few studies [1, 98] have utilized NMR to understand how the glass structure changes when two or more different modifying cations are present.

The use of two-dimensional magic angle flipping (2D MAF) NMR has been shown, in previous studies [60, 61], to give over an order of magnitude improvement in quantification of $Q^{(n)}$-species concentrations in comparison to conventional Magic Angle

Spinning (MAS) lineshape analysis. 2D MAF NMR produces a two dimensional spectrum correlating isotropic and anisotropic nuclear shielding contributions. 2D MAF NMR has been utilized by Davis et al. [7,8] to understand how the magnitude of the chemical shift anisotropy changes for samples containing different modifying cations. A clear trend was observed indicating that as cations with higher cation potential, defined as the charge of the cation divided by the atomic radius, were incorporated in the glass structure, the magnitude of the chemical shift anisotropy should linearly decrease. Using trends initially reported by Grimmer and coworkers [9,10], this change in the chemical shift anisotropy was related to a changing Si-NBO bond length. It was proposed that as cations with higher cation potential are incorporated into the glass, the Si-NBO bond length must therefore be decreasing. These studies, however, focused on analyzing silicate glasses with a single modifying cation.

When multiple network modifying cations are introduced into the glass structure the cation coordination environment near each non-bridging oxygen site is not only dependent on the total number of cations coordinated to the oxygen but also which particular cations are present near the NBO site. Therefore, the number of cation coordination environments within the glass structure is greatly increased with the addition of multiple network modifying cations. This increase in the possible number of cation coordination environments indicates that there could be multiple anisotropic nuclear shielding interactions for a particular $Q^{(n)}$ site within the glass structure.

New results are presented on a previously studied mixed potassium/magnesium tetra-silicate glass [1], of composition $K_{2x}Mg_{(1-x)}O \cdot 4SiO_2$. Farnan and coworkers determined via ^{17}O dynamic angle spinning (DAS) NMR that there was one unique cation clustering coordination environment for the $K_2O \cdot 4SiO_2$ glass and one unique

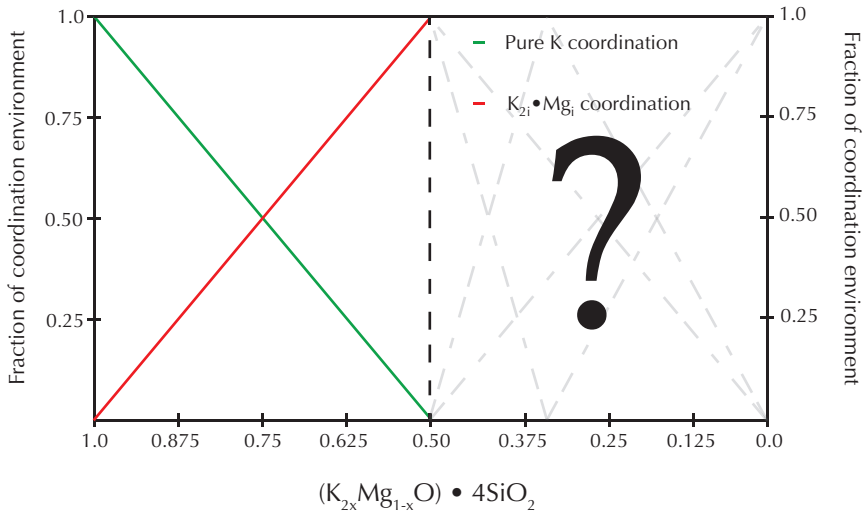

Figure 3.1: A binary model for the cation clustering coordination environments of the $K_{2x}Mg_{1-x}O \cdot 4SiO_2$ glass based on the previous ^{17}O DAS results [1]. The green line represents a pure potassium coordination environment; while, the red line represents a mixed potassium/magnesium coordination environment. The mixed coordination environment is proposed to be $K_{2i} \cdot Mg_i$. The coordination environments for the compositions $x < 0.5$ are unknown; however, several possible linear distributions of cation coordination environments are shown (gray dashed lines).

cation clustering environment for the $K_{1.0}Mg_{0.5}O \cdot 4SiO_2$ glass. Therefore, the cation clustering environment in the $K_2O \cdot 4SiO_2$ glass must be a pure potassium environment, while the cation clustering environment in the $K_{1.0}Mg_{0.5}O \cdot 4SiO_2$ glass must be a mixed potassium/magnesium coordination environment. This suggests a large amount of ordering of the network modifying cations within this mixed modified silicate glass.

In Figure 3.1, a model is presented for cation clustering coordination distributions in all compositions of the mixed potassium/magnesium tetra-silicate glass, based on these previous results. This model assumes a binary distribution of the two unique

cation clustering coordination environments; therefore, at any given composition between the x = 1 and the x = 0.5 compositions both unique cation coordination environments must be present at varying concentrations. The green line represents a pure potassium coordination environment around the non-bridging oxygen, while the red line represents a mixed potassium/magnesium coordination environment. The mixed potassium/magnesium coordination environment that is proposed is a $K_{2i} \cdot Mg_i$ coordination, where it is believed that the potassium-to-magnesium ratio is somewhat restrictive. However, the exact number of cations clustering to each non-bridging oxygen is not known. Any number of different coordination environments could be present with linear or non-linear dependencies on composition for compositions of $x < 0.5$. Therefore, only a few possible coordination environments are proposed (all linearly dependent on composition), the gray dashed lines, including distributions of pure magnesium coordination, the $K_{2i} \cdot Mg_i$ coordination environment, and a different mixed potassium and magnesium environment, $K_i \cdot Mg_i$. However, there is no evidence to suggest any particular distribution of any of these coordination environments is present in these magnesium rich compositions of the glass.

3.2 Experimental

3.2.1 Sample Preparation

Five samples were prepared with the compositions (1-z)$[K_{2x}\ Mg_{(1-x)}O \cdot 4SiO_2] \cdot zCuO$, where x = 1, 0.875, 0.75, 0.625, and 0.5 and $z \approx 0.004$. Approximately 2g of each sample was synthesized from K_2CO_3 (Aldrich, 99+%), MgO (Alfa Aesar, 99.95%), SiO_2 (Aldrich, 99.995%), and CuO (Mallinckrodt). Prior to synthesis the K_2CO_3 and MgO were placed in a dehydrating furnace at 150°C overnight to remove any

Table 3.1: Elemental analysis showing the relative population, in weight percent, of each element in each composition, errors are shown as $\pm 1\sigma$.

Glass sample	Silicon	Potassium	Magnesium
$0.9958(K_2O \cdot 4SiO_2) \cdot 0.0036CuO$	31.6 ± 3.2%	21.6 ± 2.2%	–
$0.996(K_{1.75}Mg_{0.125}O \cdot 4SiO_2) \cdot 0.004CuO$	32.1 ± 3.2%	18.8 ± 1.9%	0.92 ± 0.09%
$0.996(K_{1.5}Mg_{0.25}O \cdot 4SiO_2) \cdot 0.004CuO$	33.8 ± 3.4%	16.4 ± 1.6%	1.70 ± 0.17%
$0.9961(K_{1.25}Mg_{0.375}O \cdot 4SiO_2) \cdot 0.0039CuO$	34.4 ± 3.4%	14.7 ± 1.5%	2.77 ± 0.28%
$0.9964(K_{1.0}Mg_{0.5}O \cdot 4SiO_2) \cdot 0.0036CuO$	34.9 ± 3.5%	11.6 ± 1.2%	3.67 ± 0.37%

water from the sample. The starting materials were ground and placed in a furnace at 700°C overnight to decarbonate followed by melting at 1100°C for the x = 1 and 0.875 compositions, 1300°C for the x = 0.75 and 0.625 compositions, and 1400°C for the x = 0.5 composition for 1.5 hours. Each sample was quenched by placing the bottom of the platinum crucible in water. Each sample was ground into a powder and packed in a rotor in a nitrogen filled glove bag. We found that doping with Cu(II), which has a short enough $T_{1,e}$ to reduce the ^{29}Si T_1 without significantly reducing the ^{29}Si T_2 could aid in shortening our relaxation times. While the relaxation times for some of our undoped samples exceeded 1000s, doping with approximately 0.004 mole fraction CuO reduced the relaxation delay by a factor of approximately 20. An elemental analysis, results shown in Table 3.1, was performed by Galbraith Laboratories (Knoxville, Tennessee). Within the 95% confidence limits, the results were determined to be the same as the proposed compositions.

3.2.2 Nuclear Magnetic Resonance

All experiments were performed on a Tecmag Apollo NMR spectrometer operating at a field strength of 9.4 Tesla (79.474 MHz for ^{29}Si) using homebuilt 4mm (for the x = 1, 0.75, and 0.5 compositions) and 7mm (for the x = 0.875, 0.625 compositions) DAS probes each based on a previous design [100]. Spin lattice relaxation times, T_1, were determined by the saturation recovery experiment with a recover time t. The relaxation curves were found to be multi-exponential and were best fit with a stretched exponential function,

$$A(1 - e^{(\frac{t}{T_1})^{\beta}}), \tag{3.1}$$

where T_1 is the relaxation time for the sample. When a distribution of T_1 values is present within the relaxation of the sample a stretched exponential is used to to fit the relaxation curve due to the fact that a stretched exponential function fits a range of T_1 distributions. The β parameter is a measure of the range of the T_1 distribution, where a $\beta = 1$ is a single exponential function with one T_1 value and $\beta = 0$ is an infinite distribution of T_1 values. The single exponential fit for the x = 0.625 glass sample, shown in Figure 3.2, clearly does not represent the saturation recovery data. Therefore, the stretched exponential function was chosen to fit the saturation recovery data, shown in Figure 3.3, and was determined to be a good fit for the determination of the spin lattice relaxation times for the glass samples.

The time for 75% of the signal maximum to have recovered for each composition and the recycle delays that were used for each experiment are shown in Table 3.2. The recycle delay was initially set (for the x = 0.5 and 0.75 compositions) such that full relaxation was achieved throughout the sample. However, to further enhance

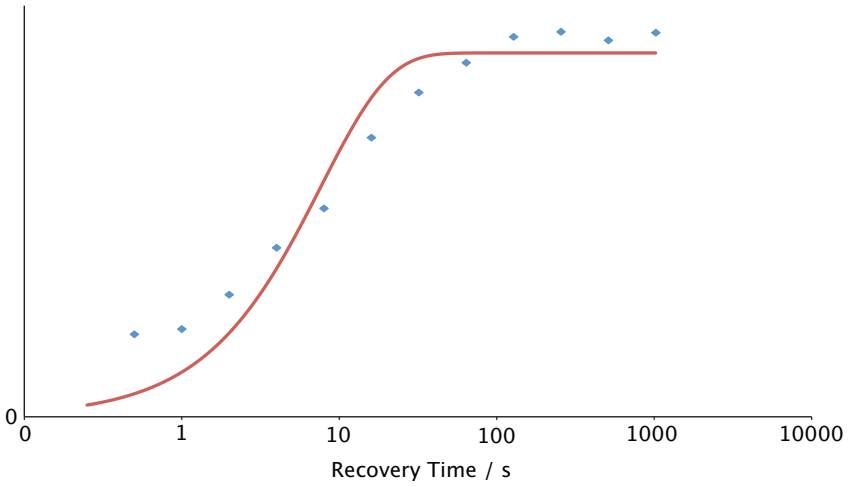

Figure 3.2: The saturation recovery data (diamonds) for the x = 0.625 sample presented with a logarithmic time axis (horizontal) fit to a single exponential function (solid line).

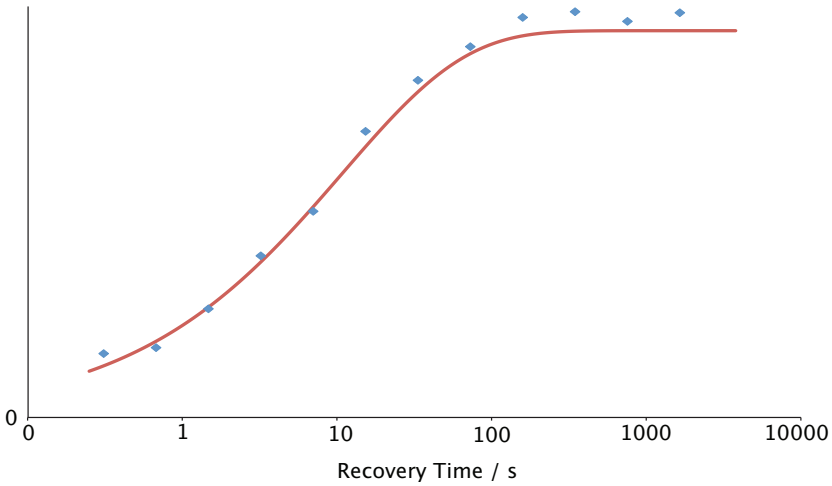

Figure 3.3: The saturation recovery data (diamonds) for the x = 0.625 sample with a logarithmic time axis (horizontal) fit to a stretched exponential function, with $\beta \approx 0.5$ (solid line).

Table 3.2: Relaxation times and recycle delays used for the 2D MAF-CPMG experiments for each composition.

Glass composition	75% time / s	Recycle delay / s
$K_2O \cdot 4SiO_2$	17.3	60.0
$K_{1.75}Mg_{0.125}O \cdot 4SiO_2$	11.3	20.0
$K_{1.5}Mg_{0.25}O \cdot 4SiO_2$	43.0	10.0 / 200
$K_{1.25}Mg_{0.375}O \cdot 4SiO_2$	20.0	7.0
$K_{1.0}Mg_{0.5}O \cdot 4SiO_2$	50.9	210

the signal-to-noise ratio (S/N) of the experiments, the recycle delay for the x = 0.75 composition ($K_{1.5}Mg_{0.25}O \cdot 4SiO_2$) was set to 10 seconds, when just over 50% of the signal maximum had recovered, to allow for a large number of scans to be performed in an identical amount of time. The two 2D MAF spectra were processed identically and a S/N enhancement of approximately 2 times was achieved. The spectra were scaled by their signal maxima, and then subtracted from one another to yield residuals that were purely noise. This gave evidence that the copper dopant was evenly distributed throughout the glass structure and that all ^{29}Si centers were being relaxed equally. Therefore, the recycle delay was truncated to shorter than full relaxation for the remaining compositions to allow for greater sensitivity and shorter experiment times.

The 2D MAF experiment correlates MAS frequencies to anisotropic frequencies obtained while spinning off the magic angle during the τ_{echo} evolution period. The detection angle, θ_R, used in this experiment is 90°, or perpendicular to the external magnetic field direction, where the averaged anisotropic frequencies are scaled by a factor of $-\frac{1}{2}$ [79]. The 2D MAF spectra were obtained using the shifted-echo MAF pulse sequence [75, 80] with CPMG [81, 82] echo-train acquisition (Figure 3.4) to

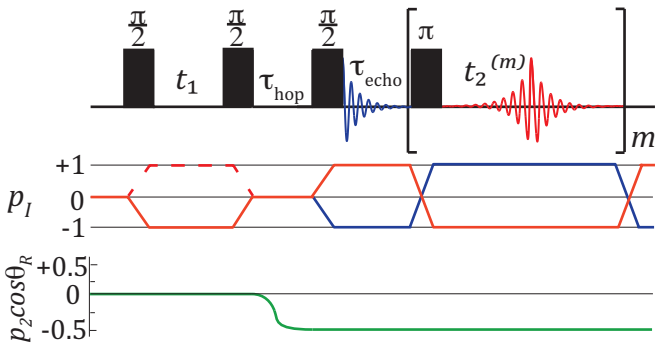

Figure 3.4: The shifted-echo Magic Angle Flipping (MAF) pulse sequence with CPMG echo train acquisition used for all experiments. The initial half-echo was acquired for only the x = 0.875 sample to enhance the signal-to-noise ratio of the experiment. Hypercomplex acquisition is performed to obtain positive and negative t_1 quadrants in the 2D time domain signal [11], as indicated by the dashed line.

enhance sensitivity due to the low isotopic abundance (∼4.7%) and NMR frequency of ^{29}Si. The original incarnation of the 2D MAF-CPMG experiment [8] detected at the magic angle due to the fact that the samples were nearly 100% ^{29}Si-enriched. When detection is performed away from the magic angle, the homonuclear ^{29}Si-^{29}Si dipolar interactions lead to a rapid dephasing of the signal and echo train. However, in the natural abundance samples that were studied for this paper detection at 90° from the external magnetic field allows for more echoes to be detected in the same period of time due the shortening of the echo time when spinning off the magic angle. The initial half-echo was acquired, for the x = 0.875 composition, processed separately and added to the rest of the data to further enhance the signal-to-noise ratio. An exponential line apodization was applied to the echo dimension of each spectrum to achieve the maximum enhancement of the sensitivity. The anisotropic dimension in

all 2D MAF figures is displayed as a pure static anisotropic dimension. This is due to a shear that was applied to the dimension to remove the isotropic contributions from the 90° spinning anisotropic lineshape, and a scaling of the frequency.

The notation, $\zeta_{\delta\ site\ m}$, will be used for the different chemical shift anisotropy values for the same $Q^{(n)}$ sites, where m indicates the arbitrary number assigned for the $Q^{(n)}$ site with that chemical shift anisotropy value.

3.3 Results and Discussion

The MAS spectrum of each composition contains a broad resonance with two distinct peaks centered near δ_{iso} = -105 ppm and δ_{iso} = -95 ppm. The presence of these two unique isotropic chemical shifts is consistent with overlapping $Q^{(4)}$ (δ_{iso} = -105 ppm) and $Q^{(3)}$ (δ_{iso} = -95 ppm) resonances. Figures 3.5–3.9 show the 2D contour plots of the MAF spectra for all compositions, where the two distinct isotropic chemical shifts can be clearly seen in the 1D projection along the isotropic dimension (vertical axis). Note that there is a clear diagonal line of noise present in all of the MAF spectra, which is due to the stepper motor that is being used for angle hopping. This characteristic noise can be ignored due to the fact that it does intersect any of the data and therefore does not affect the fitting of the 2D spectra.

Each $Q^{(n)}$-species has well-defined differences in the ^{29}Si nuclear shielding tensor, which manifest as a distinct anisotropic lineshape [60, 61]. In Figures 3.5–3.9, the MAS lineshape is clearly dominated by $Q^{(4)}$ near δ_{iso} = -105 ppm and by $Q^{(3)}$ near δ_{iso} = -95 ppm based on their distinct anisotropic linehapes found in the 90° dimension (horizontal axis). Each 2D spectrum was simulated using a Gaussian distribution of isotropic shifts for each site in the glass sample. The anisotropic lineshape for each

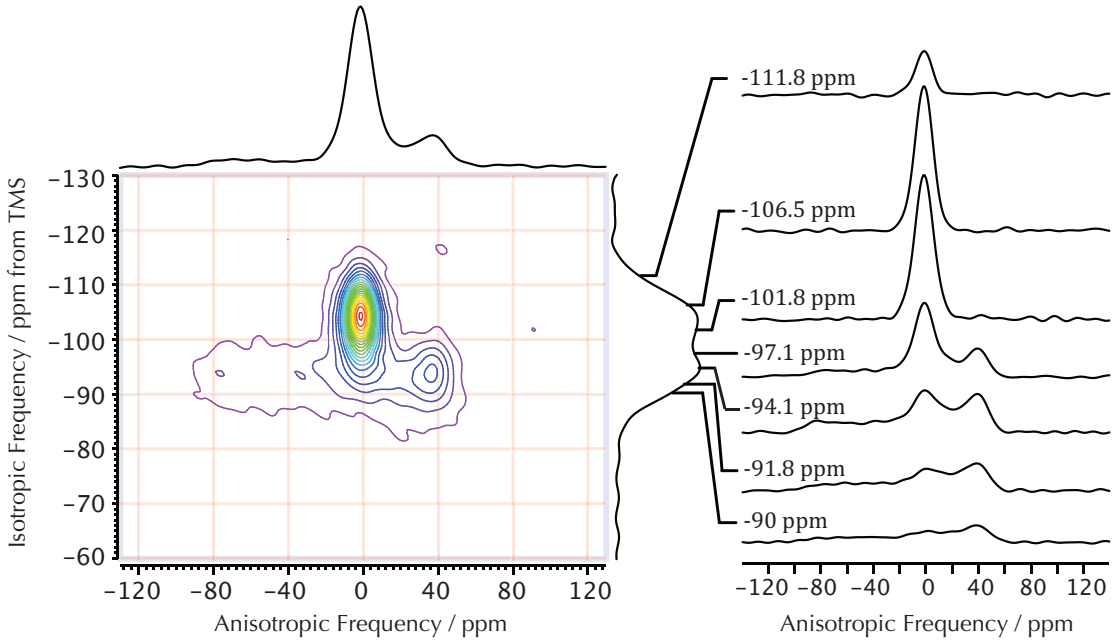

Figure 3.5: 2D MAF-CPMG spectrum of $K_2O \cdot 4SiO_2$ glass. One dimensional projections are provided onto the MAS and anisotropic dimensions. Selected cross sections of the anisotropic dimension are presented to the right of the 2D spectrum. The anisotropic dimension shown is obtained as a 90° spinning dimension and a shear is applied and the frequencies are scaled to yield a purely static anisotropic lineshape.

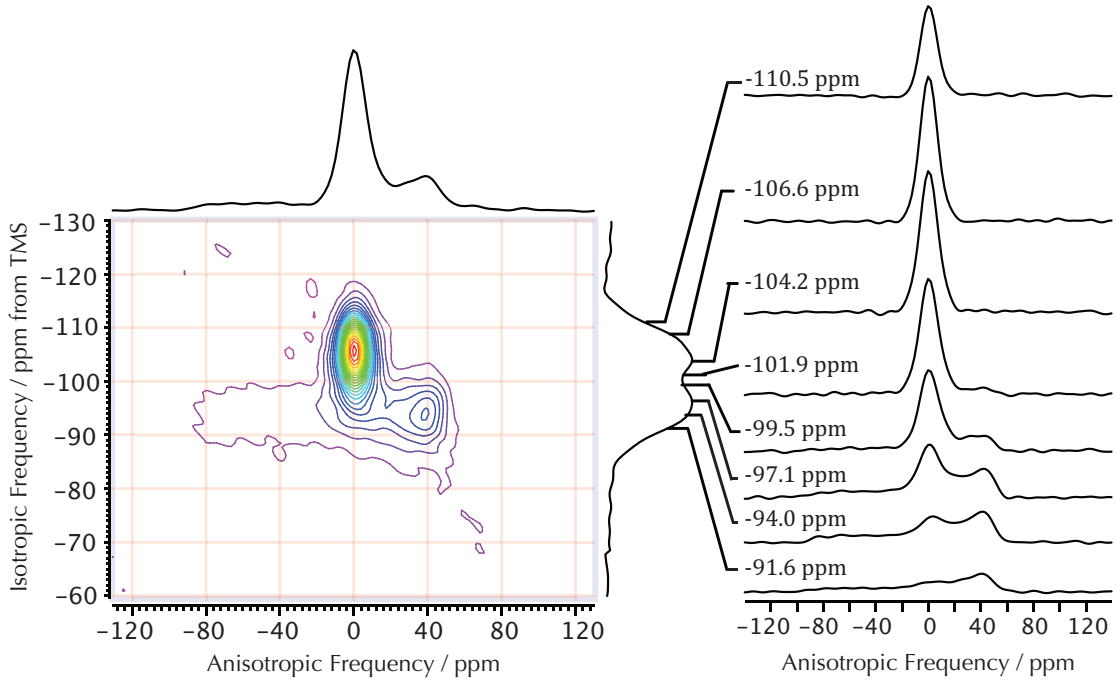

Figure 3.6: 2D MAF-CPMG spectrum of $K_{1.75}Mg_{0.125}O \cdot 4SiO_2$ glass. One dimensional projections are provided onto the MAS and anisotropic dimensions. Selected cross sections of the anisotropic dimension are presented to the right of the 2D spectrum. The anisotropic dimension shown is obtained as a 90° spinning dimension and a shear is applied and the frequencies are scaled to yield a purely static anisotropic lineshape.

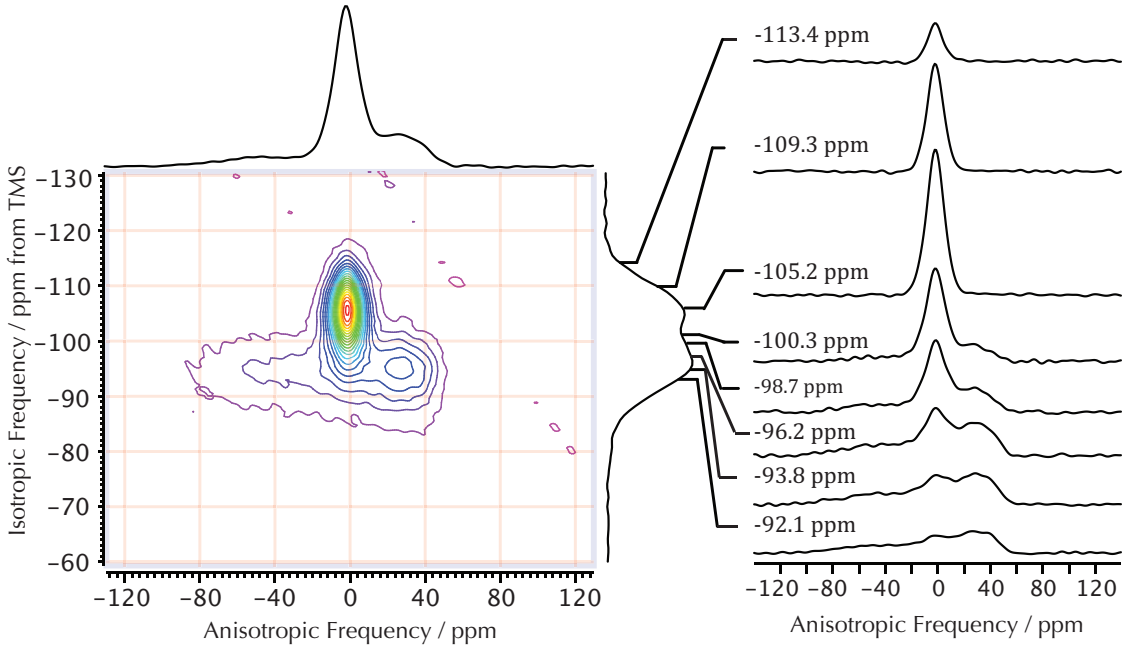

Figure 3.7: 2D MAF-CPMG spectrum of $K_{1.5}Mg_{0.25}O \cdot 4SiO_2$ glass when a recycle delay of 10 seconds was used. The residuals of the experiment where the recycle delay was set to 200 seconds and the experiment shown were found to be noise. One dimensional projections are provided onto the MAS and anisotropic dimensions. Selected cross sections of the anisotropic dimension are presented to the right of the 2D spectrum. The anisotropic dimension shown is obtained as a 90° spinning dimension and a shear is applied and the frequencies are scaled to yield a purely static anisotropic lineshape.

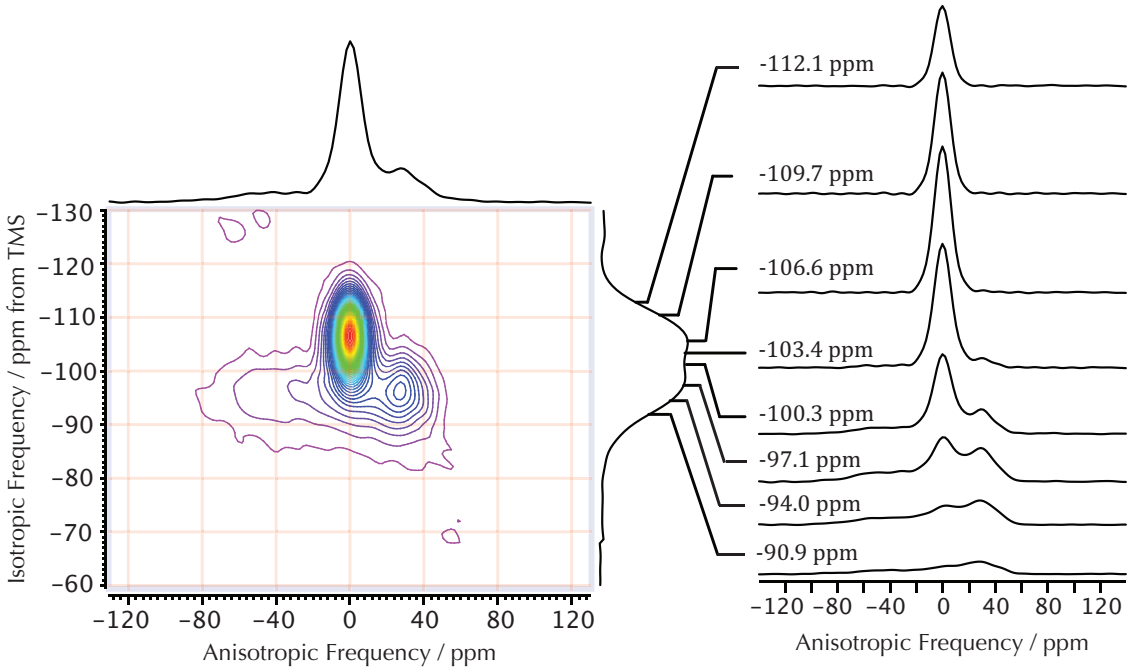

Figure 3.8: 2D MAF-CPMG spectrum of $K_{1.25}Mg_{0.375}O \cdot 4SiO_2$ glass. One dimensional projections are provided onto the MAS and anisotropic dimensions. Selected cross sections of the anisotropic dimension are presented to the right of the 2D spectrum. The anisotropic dimension shown is obtained as a 90° spinning dimension and a shear is applied and the frequencies are scaled to yield a purely static anisotropic lineshape.

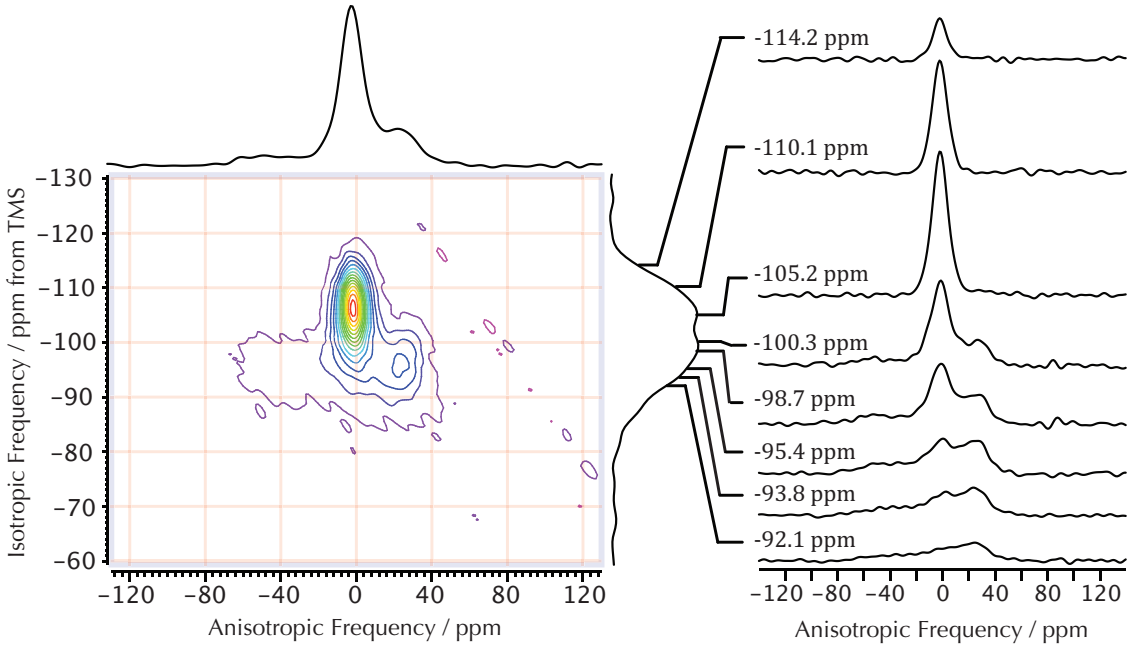

Figure 3.9: 2D MAF-CPMG spectrum of $K_{1.0}Mg_{0.5}O \cdot 4SiO_2$ glass. One dimensional projections are provided onto the MAS and anisotropic dimensions. Selected cross sections of the anisotropic dimension are presented to the right of the 2D spectrum. The anisotropic dimension shown is obtained as a 90° spinning dimension and a shear is applied and the frequencies are scaled to yield a purely static anisotropic lineshape.

$Q^{(n)}$ site was modeled by several parameters: (1) a Gaussian line broadening, (2) the overall isotropic chemical shift, δ_{iso}, (3) the principal components of the chemical shift tensor, δ_{xx}, δ_{yy}, and δ_{zz}, (4) the integrated intensity of each $Q^{(n)}$ site, and (5) the isotropic shift distribution of each $Q^{(n)}$ site ($\langle\delta_{iso}\rangle$ and the width). No constraints were placed on the parameters that were being used to model the anisotropic lineshape for each $Q^{(n)}$ site. Therefore, all of the parameters varied freely throughout the simulations.

The best fit values for the chemical shift anisotropy for each $Q^{(n)}$ site and the relative fraction for each $Q^{(n)}$ site are shown in Table 3.4. While, the mean and width of the isotropic chemical shift distributions for each $Q^{(n)}$ site are shown in Table 3.5. Previous work by Farnan et al. [1] suggested that the x = 1 and 0.5 compositions had a single unique chemical shift anisotropy; therefore, the x = 1 and 0.5 spectra were simulated assuming a two site model, one $Q^{(3)}$ and one $Q^{(4)}$ site. The chemical shift anisotropy for the $Q^{(4)}$ was assumed to be nearly zero and was held constant across all isotropic shift values. The chemical shift anisotropy of the $Q^{(3)}$ site was also held constant across the isotropic chemical shift distribution; however, the anisotropy, ζ_δ, in the x = 1 composition was determined to be -84.7 $\pm$ 0.1 ppm, while for the x = 0.5 composition it was found to be -60.4 $\pm$ 0.2 ppm, as shown in Table 3.4. The chemical shift anisotropy for the $Q^{(3)}$ site associated with a pure potassium clustering environment is labelled as $\zeta_{\delta\ site\ 1}$; whereas, the mixed potassium/magnesium clustering environment is labelled as $\zeta_{\delta\ site\ 2}$.

Therefore, a distinct chemical shift anisotropy, ζ_δ, for the x = 1 and 0.5 compositions was found, in agreement with the previous ^{17}O results [1]. The x = 0.5 sample, which has a composition of $K_{1.0}Mg_{0.5}O \cdot 4SiO_2$, has equal by charge, populations

of potassium and magnesium. Therefore, the cation clustering coordination in the x = 0.5 composition is believed to be the $K_{2i} \cdot Mg_i$ coordination environment that was proposed earlier. This mixed cation clustering environment has a potassium-to-magnesium ratio that is thought to be somewhat restrictive; however, the exact number of modifying cations is not known. The chemical shift anisotropy, ζ_δ, for the x = 1 ($K_2O \cdot 4SiO_2$) and 0.5 ($K_{1.0}Mg_{0.5}O \cdot 4SiO_2$) compositions were determined to be in agreement with previously reported trends [7, 99] for varying network modifying cation potential. The chemical shift anisotropy for the $K_{2i} \cdot Mg_i$ coordination environment was determined to be between previous results for pure potassium and pure magnesium silicate glasses. Therefore, the Si-NBO bond distance for the $K_{2i} \cdot Mg_i$ coordination environment is believed to be between the Si-NBO bond distance for pure potassium and pure magnesium silicate glasses.

According to the earlier proposed binary model the x = 0.875 ($K_{1.75}Mg_{0.125}O \cdot 4SiO_2$), x = 0.75 ($K_{1.5}Mg_{0.25}O \cdot 4SiO_2$), and x = 0.625 ($K_{1.25}Mg_{0.375}O \cdot 4SiO_2$) compositions are believed to have two distinct $Q^{(3)}$ sites with a differing relative population in each distinct $Q^{(3)}$ site. These compositions were simulated (Figures 3.10A–3.12A) with the same two site model (one $Q^{(4)}$ site and one $Q^{(3)}$ site) as the x = 1 and 0.5 compositions; a three site model (one $Q^{(4)}$ site and two $Q^{(3)}$ sites) was also employed, Figures 3.10B–3.12B. The three site simulation was determined to be a better fit for the experimental data than the two site model using the F-test [101]. The F-test that was used to compare the two different models was defined as,

$$F = \frac{(\chi_1^2 - \chi_2^2)/(P_2 - P_1)}{\chi_2^2/(n - P_2)}, \quad P_2 > P_1, \tag{3.2}$$

where χ_1^2 is the chi-squared value for the two site model, χ_2^2 is the chi-squared value for the three site model, P_1 is the number of parameters used to constrain the two site

Table 3.3: The F_{calc} values for the two and three site model for the x = 0.875, 0.75, and 0.625 compositions.

Glass composition	χ^2_1	χ^2_2	F_{calc}	$F_{critical}$
$K_{1.75}Mg_{0.125}O \cdot 4SiO_2$	81428	77414	19.2	1.0
$K_{1.5}Mg_{0.25}O \cdot 4SiO_2$	105318	94618	41.9	1.0
$K_{1.25}Mg_{0.375}O \cdot 4SiO_2$	166042	120422	140.4	1.0

model, P_2 is the number of parameters for the three site model, and n is the number of bootstrap simulations used for both models. The number of parameters for the two site model was 14 (P_1), and the number of parameters used in the three site model was 18 (P_2). The calculated F values are shown in Table 3.3. The three site model is shown to be a significantly better fit than the two site model based on the F-test. The comparison of the two and three site models for the x = 0.75 sample in Figure 3.11 clearly shows the deficiencies of the two site model. Therefore, by assuming a three site model for the x = 0.875, 0.75, and 0.625 compositions and using the chemical shift anisotropy parameters from the x = 1 and 0.5 compositions as a starting point, each spectrum was fit, shown in Table 3.4.

The chemical shift anisotropy for each site in the compositions was found to be similar to the original starting parameters; however, due to factors that were not accounted for, such as non-identical experimental conditions, or slight disparities in composition, the ζ_δ for each site in each composition were not found to be identical. However, it is believed that the chemical shift anisotropy for the distinct $Q^{(3)}$ sites in each composition correspond to the same cation clustering coordination environment. The large error that is present on $\zeta_{\delta\ site\ 2}$ for the x = 0.875 composition is

Table 3.4: The reduced-chi-squared value, χ^2_ν, the chemical shift anisotropy, ζ_δ for both sites, the relative fraction for the $Q^{(4)}$ and $Q^{(3)}$ sites in each glass, and the relative fraction of both $Q^{(3)}$-species within each glass composition. The errors reported are $\pm 1\sigma$ and were determined by bootstrap resampling [12] during the simualtions.

Glass composition	χ^2_ν	$\zeta_{\delta\ site\ 1}$ / ppm	$\zeta_{\delta\ site\ 2}$ / ppm	Relative $Q^{(3)}$ fraction	Relative $Q^{(4)}$ fraction	Relative fraction of $Q^{(3)}$ for site 1	Relative fraction of $Q^{(3)}$ for site 2
$K_2O \cdot 4SiO_2$	1.58 ± 0.02	-84.7 ± 0.1	–	0.464 ± 0.003	0.536 ± 0.002	1	–
$K_{1.75}Mg_{0.125}O \cdot 4SiO_2$	1.35 ± 0.03	-85.5 ± 1.1	-63.1 ± 4.8	0.49 ± 0.04	0.51 ± 0.04	0.79 ± 0.06	0.21 ± 0.06
$K_{1.5}Mg_{0.25}O \cdot 4SiO_2$	1.68 ± 0.02	-86.2 ± 0.4	-58.6 ± 0.3	0.508 ± 0.005	0.492 ± 0.005	0.512 ± 0.005	0.488 ± 0.004
$K_{1.25}Mg_{0.375}O \cdot 4SiO_2$	2.19 ± 0.17	-87.5 ± 0.6	-61.9 ± 0.3	0.47 ± 0.01	0.53 ± 0.01	0.252 ± 0.006	0.75 ± 0.02
$K_{1.0}Mg_{0.5}O \cdot 4SiO_2$	1.44 ± 0.02	–	-60.4 ± 0.2	0.458 ± 0.003	0.542 ± 0.004	–	1

Table 3.5: The mean and width reported with $\pm 1\sigma$ errors determined from bootstrap resampling simulations [12] for the isotropic shift distributions of the $Q^{(n)}$ sites within each glass structure.

Glass composition	$\langle \delta_{iso}^{(4)} \rangle$ / ppm	Width / ppm	$\langle \delta_{iso,\ site\ 1}^{(3)} \rangle$ / ppm	Width / ppm	$\langle \delta_{iso,\ site\ 2}^{(3)} \rangle$ / ppm	Width / ppm
x = 1	-103.89 ± 0.08	7.13 ± 0.01	-93.29 ± 0.04	5.85 ± 0.02	–	–
x = 0.875	-105.4 ± 0.1	5.36 ± 0.04	-93.4 ± 0.2	4.8 ± 0.7	-96.0 ± 1.0	3.3 ± 0.2
x = 0.75	-105.50 ±0.09	5.10 ± 0.01	-94.1 ± 0.2	4.60 ± 0.04	-95.3 ± 0.3	4.63 ± 0.04
x = 0.625	-106.48 ± 0.06	5.37 ± 0.01	-93.1 ± 0.6	6.5 ± 0.2	-96.4 ± 0.2	4.75 ± 0.06
x = 0.5	-106.3 ± 0.2	5.32 ± 0.02	–	–	-95.7 ± 0.3	5.24 ± 0.04

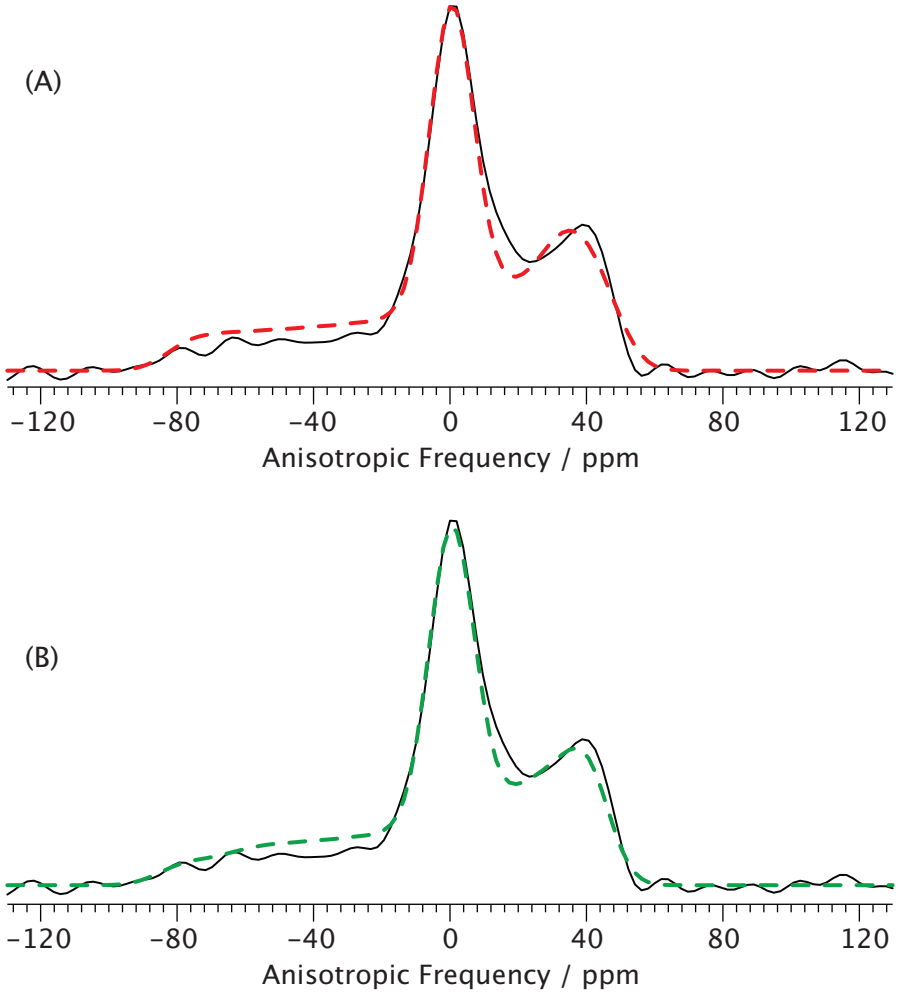

Figure 3.10: 1D cross section of the 2D MAF-CPMG spectrum of $K_{1.75}Mg_{0.125}O \cdot 4SiO_2$ glass at δ_{iso} = -97.9 ppm with respect to TMS. The experimental (solid line) cross section is shown with simulated cross sections (dashed lines) when a two site model (one $Q^{(4)}$ and one $Q^{(3)}$ site) was used (above, red line) and when a three site model (one $Q^{(4)}$ and two $Q^{(3)}$ sites) was used (below, green line). The anisotropic dimension shown is obtained as a 90° spinning dimension and a shear is applied and the frequency is scaled to yield a purely static anisotropic lineshape.

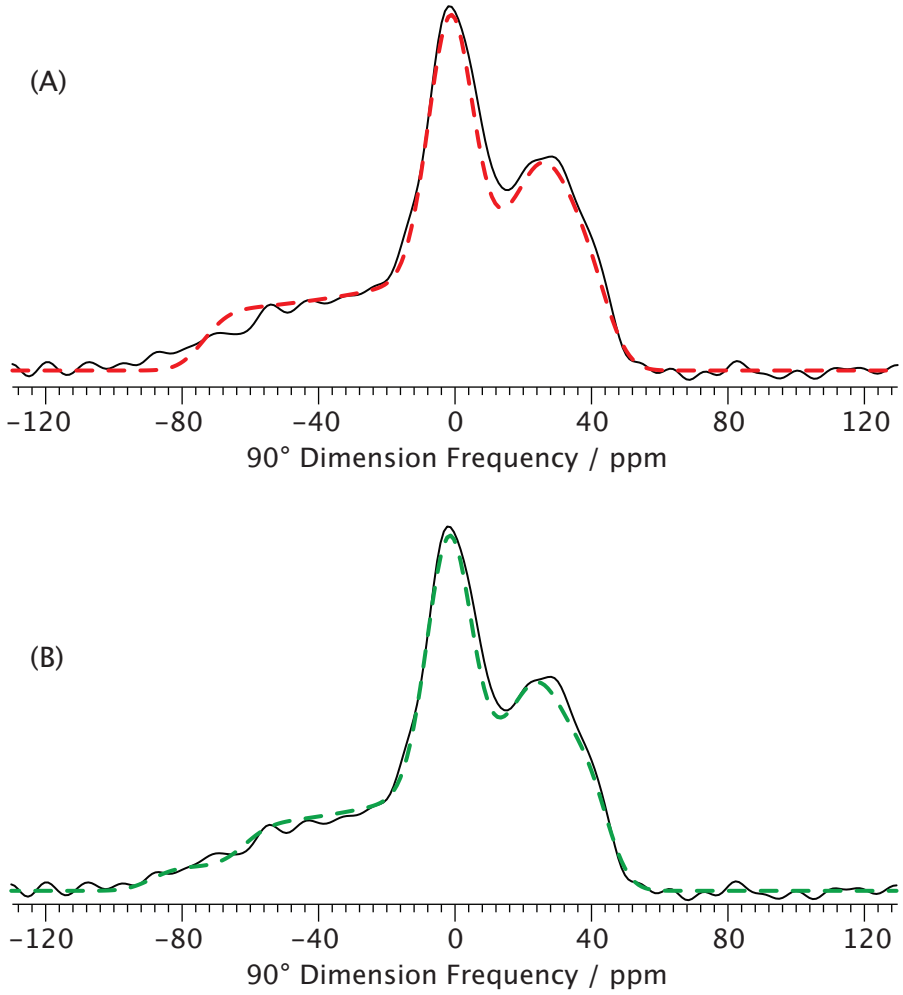

Figure 3.11: 1D cross section of the 2D MAF-CPMG spectrum of $K_{1.5}Mg_{0.25}O \cdot 4SiO_2$ glass at δ_{iso} = -97.0 ppm with respect to TMS. The experimental (solid line) cross section is shown with simulated cross sections (dashed lines) when a two site model (one $Q^{(4)}$ and one $Q^{(3)}$ site) was used (above, red line) and when a three site model (one $Q^{(4)}$ and two $Q^{(3)}$ sites) was used (below, green line). The dimension that is displayed is a pure static anisotropic dimension due to the shear applied to the obtained 90° spinning dimension and a scaling of the frequency.

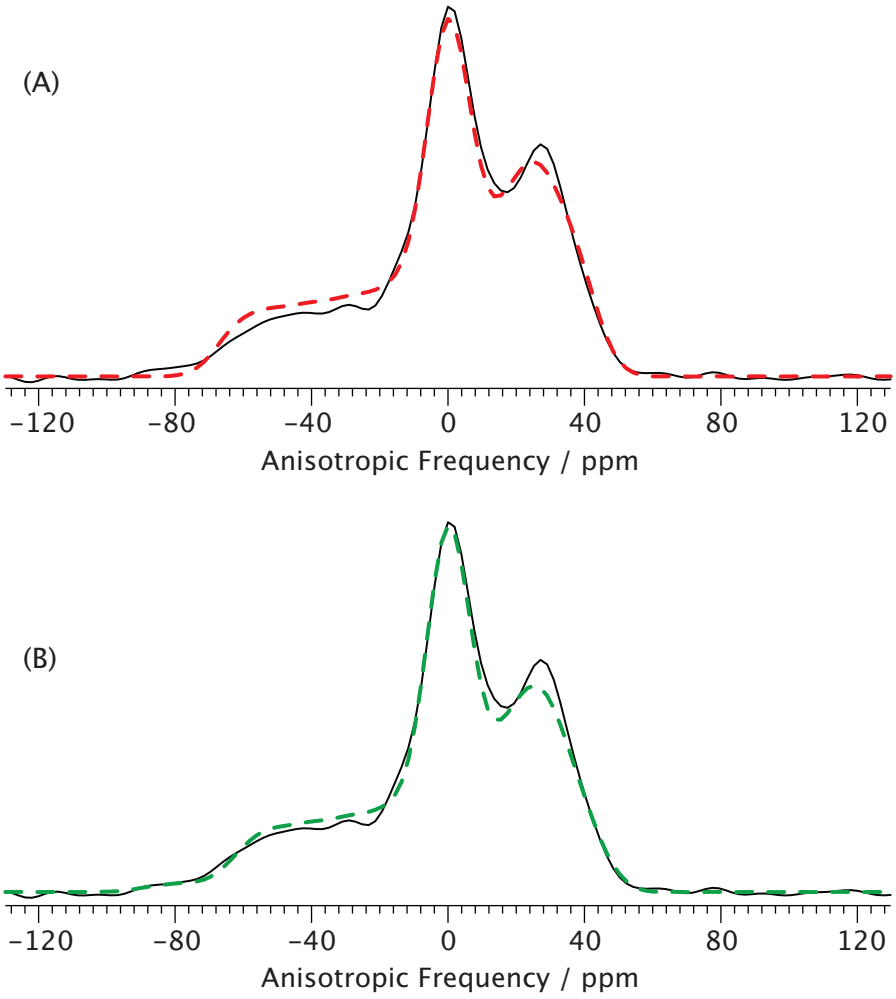

Figure 3.12: 1D cross section of the 2D MAF-CPMG spectrum of $K_{1.25}Mg_{0.375}O \cdot 4SiO_2$ glass at δ_{iso} = -97.9 ppm with respect to TMS. The experimental (solid line) cross section is shown with simulated cross sections (dashed lines) when a two site model (one $Q^{(4)}$ and one $Q^{(3)}$ site) was used (above, red line) and when a three site model (one $Q^{(4)}$ and two $Q^{(3)}$ sites) was used (below, green line). The anisotropic dimension shown is obtained as a 90° spinning dimension and a shear is applied and the frequency is scaled to yield a purely static anisotropic lineshape.

likely due to the low fraction of $Q^{(3)}_{site\ 2}$ within the composition and the fact that its narrower lineshape is difficult to model underneath the wider and more abundant $Q^{(3)}_{site\ 1}$ lineshape. Therefore, the fitting of the three site model was most difficult to implement on the x = 0.875 composition. The low fraction of the wider $Q^{(3)}_{site\ 1}$ lineshape in the x = 0.625 sample can be fit with relative ease, as evidenced by the small errors in Table 3.4. The x = 0.625 sample can be fit with ease due to the fact the the least abundant $Q^{(3)}$ lineshape is the wider lineshape corresponding to a pure potassium clustering environment and therefore it is not hidden underneath a wider more abundant lineshape like the fit for the x = 0.875 sample.

The relative populations of the two $Q^{(3)}$ sites were calculated based on the integrated intensity of each $Q^{(n)}$ lineshape from the fit and are shown in Table 3.4. The errors for all parameters were calculated using the bootstrap resampling method during the simulations [12] and are reported as one standard deviation ($\pm 1\sigma$). The relative populations of the two distinct $Q^{(3)}$ sites in each composition were determined to be in good agreement with the binary model for the cation clustering environments around each non-bridging oxygen, as shown in Figure 3.13. Therefore, the network modifying cations coordinated near the NBO sites in this mixed magnesium/potassium tetra-silicate glass for all compositions, $1 \geq x \geq 0.5$, are believed to be found as a binary mixture of a pure potassium coordination environment and a $K_{2i} \cdot Mg_i$ mixed coordination environment. This suggests, in agreement with previous result, a considerable amount of ordering in the cation clustering within the glass structure.

In Figure 3.14, the ab initio calculations and the 2D MAF experimental results are combined to create a model for the cation clustering environments within this

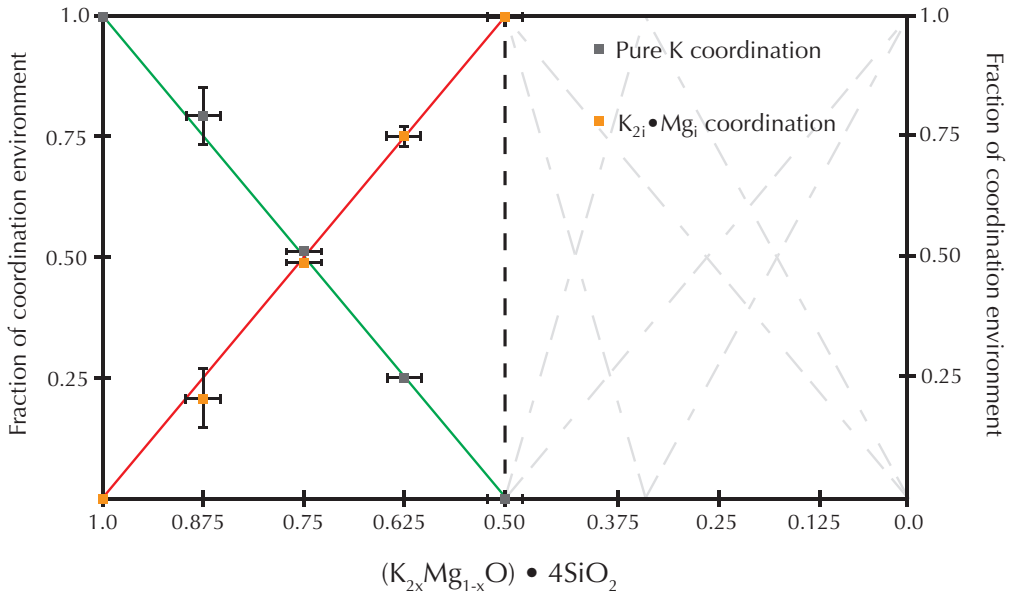

Figure 3.13: The binary model for the cation clustering coordination environments with the MAF results for each composition. The error bars reported for the fraction of each cation clustering environment (vertical dimension) are $\pm 1\sigma$ and are taken from Table 3.4. The points with no error bars have errors that are smaller than the size of the point and therefore the error bars are not visible. The error bars reported for the composition (horizontal axis) are from the elemental analysis of the glass samples.

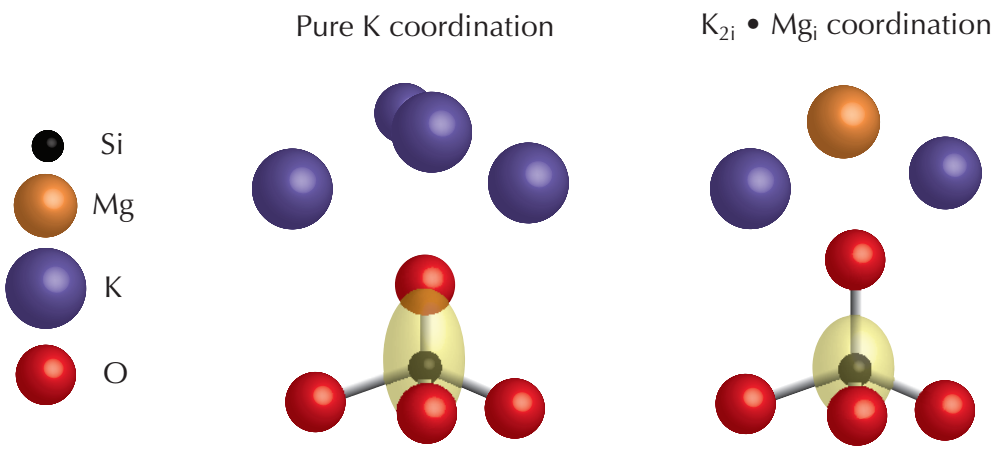

Figure 3.14: A model is presented for the cation clustering in the glass. The nuclear shielding tensors are represented based on the relative Si-NBO bond distance that is expected for each clustering environment determined from their chemical shift anisotropy from Table 3.4. A coordination of four (Pure K) and three (mixed K/Mg) modifier cations was chosen to represent the clustering environment based on an analysis of Pauling's Rules [102] and to keep a charge balance for the cation clustering environments. However, there are probably various numbers of cations modifying each non-bridging oxygen.

mixed potassium/magnesium glass composition. The nuclear shielding tensors are shown based on the relative Si-NBO bond distance that is determined based on the chemical shift anisotropy determined from the MAF results. The number of modifier cations was chosen to be four and three based on an analysis of the oxygen anions using Pauling's rules [102] and to create a balance of the overall charge of the clustering environments. However, there could be various numbers of modifier cations near each non-bridging oxygen.

3.4 Conclusions

A range of compositions of a mixed potassium/magnesium tetra-silicate glass was synthesized and analyzed by natural abundance ^{29}Si 2D MAF NMR. The spectral analysis yielded a close to equal distribution of $Q^{(3)}$ and $Q^{(4)}$ sites within the glass as expected from the stoichiometry of the glass. Two distinct chemical shift anisotropy patterns were determined from the simulations, centered near -85 ppm, corresponding to pure potassium region of cation clustering, and approximately -60 ppm, corresponding to a mixed potassium/magnesium region of cation clustering, which was proposed as a $K_{2i} \cdot Mg_i$ coordination environment. This was in agreement with the previous ^{17}O DAS results. The relative populations of each $Q^{(3)}$ site within each compositions were found to be in agreement with the binary model proposed in this paper. Therefore, a large amount of order is present within the glass relating to how the network modifying cations cluster near the non-bridging oxygens. The chemical shift anisotropy observed for the two unique $Q^{(3)}$ sites was consistent with established trends in which the ^{29}Si nucleus becomes more shielded with decreasing silicon non-bridging oxygen bond distance, causing an increase in chemical shift anisotropy when a lower field strength modifier cation is coordinated to the non-bridging oxygen.

BIBLIOGRAPHY

[1] I. Farnan, P. J. Grandinetti, J. H. Baltisberger, J. F. Stebbins, U. Werner, M. A. Eastman, A. Pines, Quantification of the disorder in network-modified silicate glasses, Nature 358 (1992) 31–35.

[2] W. H. Zachariasen, The atomic structure in glass, J. Am. Chem. Soc. 54 (1932) 3841–3851.

[3] B. E. Warren, J. Biscoe, Fourier analysis of X-ray patterns of soda-silica glass, J. Am. Ceram. Soc. 21 (1938) 259–265.

[4] G. N. Greaves, Exafs and the structure of glass, J. Non-Cryst. Solids 71 (1985) 203–217.

[5] J. Neuefeind, K.-D. Liss, Bond angle distribution in amorphous germania and silica, Berichte der Bunsen-Gesellschaft-Phys. Chem. Chem. Phys. 100 (8) (1996) 1341–1349.

[6] E. Schneider, J. F. Stebbins, A. Pines, Speciation and local structure in alkali and alkaline earth silicate glasses: Constraints from ^{29}Si NMR spectroscopy, J. Non Cryst. Solids 89 (1987) 371–383.

[7] M. Davis, D. Kaseman, S. Parvani, K. Sanders, P. Grandinetti, P. Florian, D. Massiot, $Q^{(n)}$-species distribution in K_2O $2SiO_2$ by ^{29}Si Magic Angle Flipping NMR, J. Phys. Chem. A 114 (17) (2010) 5503–5508.

[8] M. Davis, K. J. Sanders, P. J. Grandinetti, S. J. Gaudio, S. Sen, Structural investigations of magnesium silicate glasses by ^{29}si magic-angle flipping nmr, J. Non. Cryst. Solids 357 (2011) 2787–2795.

[9] A. R. Grimmer, E. F. Gechner, G. Molgedey, High resolution ^{29}Si NMR in solid silicates. correlations between shielding tensor and Si-O bond length, Chem. Phys. Lett. 77 (1981) 331–335.

[10] A. R. Grimmer, Correlation between individual Si-O bond lengths and the principal values of the ^{29}Si chemical-shift tensor in solid silicates, Chem. Phys. Lett. 119 (1985) 416–420.

[11] R. R. Ernst, G. Bodenhausen, A. Wokaun, Principles of Nuclear Magnetic Resonance in One and Two Dimensions, Oxford, Oxford, 1987.

[12] B. Efron, Bootstrap methods: Another look at the jackknife, The Annals of Statistics 7 (1) (1979) 1–26.

[13] B. O. Mysen, P. Richet, Silicate Glasses and Melts, Properties and Structure, Elsevier, 2005.

[14] A. K. Varshneya, Fundamentals of Inorganic Glasses, Academic Press Inc., 1250 Sixth Avenue, San Diego, CA 92101, 1994.

[15] A. D. Wilson, B. E. Kent, The glass-ionomer cement, a new translucent dental filling material, J. Appl. Chem. Biotechn. 21 (11) (1971) 313.

[16] P. Zhang, A. N. Klymachyov, S. Brown, J. G. Ellington, P. J. Grandinetti, Solid-state ^{13}C NMR investigations of the glycosidic linkage in α-α' trehalose, Solid State NMR 12 (1998) 221–225.

[17] C. Zerwick, A Short History of Glass, The Corning Museum of Glass, Corning, New York, 1980.

[18] J. Dixon, J. Cann, C. Renfrew, Obsidian and the origins of trade, Scientific Anerican 29 (1968) 38–46.

[19] J. Zarzycki, Glasses and the Vitreous State, Cambridge Unversity Press, Cambridge, 1991.

[20] H. Tait, Five Thousand Years of Glass, British Museum Press, London, England, 1991.

[21] M. Bimson, I. C. Freestone, Early Vitreous Materials, Vol. 56, British Museum, 1987.

[22] A. Oppenheim, R. H. Brill, D. Barage, A. von Saldern, Glass and Glassmaking in Ancient Mesopotamia. An edition of the cuneform texts which contain instructions for glassmakers, with a catlogue of surviving objects, The Corning Museum of Glass Press, Corning, New York, 1970.

[23] D. Grose, Innovation and change in ancient technologies: The anomalous case of the roman glass industry, Ceramics and Civilization 3 (1986) 65–79.

[24] G. Eisen, The origin of glass blowing, Am. J. Archeaol. 20 (2) (1916) 134–143.

[25] R. Clay, T. Court, The History of the Microscope, Charles Grifin, London, England, 1932.

[26] N. Platakis, H. Gatos, New flask evaporation method imporves film preparation, Journal of the Electrochemistry Society 123 (1976) 1409.

[27] P. Davidse, L. Maissel, Dielectric flims through rf sputtering, Journal of Applied Physics 37 (1966) 574.

[28] Y. Wada, M. Ashikawa, Oxidation characteristics of nitrogen implanted silicon, Japan Journal of Applied Physics 15 (1976) 1725.

[29] W. Kern, Chemical vapor-deposition systems for glass passivation of integrated circuits, Solid State Technologies 18 (1975) 25.

[30] W. Kern, G. Schnable, A. Fischer, Passivation coatings of silicon devices, RCA Review 37 (1976) 3.

[31] W. Kern, R. Rosler, Advances in deposition processes for passivation films, Journal of Vacuum Science Technologies 14 (1977) 1082.

[32] D. Secrist, J. Mackenzie, Solid state equilibria in systems lithium-carbon and lithium-boron, Bulletin of the American Ceramics Society 45 (1966) 784.

[33] G. Scherer, Sintering of low density glasses, Journal of the American Ceramics Society 60 (1977) 236.

[34] W. Primak, Electron bombardment investigation of dilatation in pile-exposed vitreous silica, Bulletin of of the American Physical Society 13 (1968) 74.

[35] H. Dislich, Glastechn, Ber 44 (1971) 1.

[36] G. McCarthy, R. Roy, Gel route to homogenous glass preparation .2 gelling and desiccation, Journal of American Ceramics Society 54 (1971) 639.

[37] R. A. Weeks, D. Kinser, G. Kordas, 1st international conference on effects of modes of formation on the structure of glass, Journal of Non-Crystalline Solids 71 (1985) 1–456.

[38] R. A. Weeks, D. Kinser, 2nd international conference on effects of modes of formation on the structure of glass, Diffusion and Defect Data 53-4 (1985) 9–20.

[39] I. Fanderlik, Silica Glass and Its Applications, Elsevier, Amsterdam, Netherlands, 1990.

[40] R. Mozzi, B. Warren, Structure of vitreous silica, Journal of Appl. Cryst. 2 (1969) 164–172.

[41] T. Uchino, Y. Tokuda, T. Yoko, Vibrational dynamics of defect modes in vitreous silica, Phys. Rev. B 58 (1998) 5322–5328.

[42] P. J. Bray, NMR studies of the structures of glasses, J. Non Cryst. Solids 95 (1987) 45–60.

[43] W. G. Dorfeld, Structural thermodynamics of alkali silicates, Phys. Chem. Glasses 29 (1988) 179.

[44] R. Dupree, D. Holland, P. W. McMillan, R. F. Pettifer, The structure of soda-silica glasses: A MAS NMR study, J. Non-Cryst. Solids 68 (1984) 399.

[45] P. F. McMillan, G. H. Wolf, Vibrational spectroscopy of silicate liquids, in: J. F. Stebbins, P. F. McMillan, D. B. Dingwell (Eds.), Structure , Dynamics and Properties of Silicate Melts, Vol. 32 of Reviews in Mineralogy, Mineralogical Society of America, Washington, DC, 1995, pp. 505–562.

[46] J. F. Mammone, S. K. Sharma, M. F. Nicol, Ring structures in silica glass-a raman spectroscopic investigation, EOS 62 (1981) 425.

[47] F. L. Galeener, Planar rings in glasses, Solid State Communications 44 (1982) 1037.

[48] R. Barrio, F. Galeener, E. Martinez, R. Elliot, Regular ring dynamics in ax2 tetrahedral glasses, Physics Review B 48 (1993) 15672–15689.

[49] B. O. Mysen, L. W. Finger, D. Virgo, F. A. Seifert, Curve-fitting of raman spectra of silicate glasses, Am. Miner. 67 (1982) 686–695.

[50] W. J. Malfait, W. E. Halter, Y. Morizet, B. H. Meier, R. Verel, Structural control on bulk melt properties: Single and double quantum ^{29}Si NMR spectroscopy on alkali-silicate glasses, Geochimica et Cosmochimica Acta 71 (2007) 6002–6018.

[51] R. J. P. Lyon, Infra-red confirmation of 6-fold co-ordination of silicon in stishovite, Nature 196 (1962) 266.

[52] J. G. E. Brown, F. Farges, G. Calas, X-ray scattering and x-ray spectroscopy studies of silicate melts, in: J. F. Stebbins, P. F. McMillan, D. B. Dingwell (Eds.), Structure , Dynamics and Properties of Silicate Melts, Vol. 32 of Reviews in Mineralogy, Mineralogical Society of America, Washington, DC, 1995, pp. 317–410.

[53] J. Zarzycki, Sur l'angle de la liaison si–o–si de la silice vitreuse et celui de la liaison ge–o–ge de l'oxyde de germanium vitreux ou liquide, Verres et Refractaires 11 (1957) 3.

[54] J. Zarzycki, Synthesis of glasses by hot-pressing of gels, Journal of Material Science 6 (1971) 130.

[55] J. Zarzycki, Congres intern. de verre, Trav. IV Szkice i materiały historyczne z XIX i XX wieku (1956) 323.

[56] B. E. Warren, H. Krutter, O. Morningstar, Fourier analysis of x-ray patterns of vitreous SiO_2 and B_2O_3, J. Am. Ceram. Soc. 19 (1936) 202–206.

[57] A. C. Wright, Neutron scattering from vitreous silica. V. the structure of vitreous silica: What have we learned from 60 years of diffraction studies?, J. Non Cryst. Solids 179 (1994) 84–115.

[58] A. C. Wright, Neutron and x-ray amorphography, in: C. J. Simmons, O. H. El-Bayoumi (Eds.), Experimental Techniques of Glass Science, The American Ceramic Society, Westerville, OH, 1993, p. 205.

[59] E. Henniger, R. Buschert, Atomic structure and correlation in liquid binaries by x-ray and neutron diffraction with application to nak, Journal of Chemical Physics 44 (1966) 1758.

[60] P. Zhang, C. Dunlap, P. Florian, P. J. Grandinetti, I. Farnan, J. F. Stebbins, Silicon site distributions in an alkali silicate glass derived by two-dimensional ^{29}Si nuclear magnetic resonance, J. Non. Cryst. Solids 204 (1996) 294–300.

[61] P. Zhang, P. J. Grandinetti, J. F. Stebbins, Anionic species determination in $CaSiO_3$ glass using two-dimensional ^{29}Si NMR, J. Phys. Chem. B 101 (20) (1997) 4004–4008.

[62] J. F. Emerson, P. E. Stallworth, P. J. Bray, High-field ^{29}Si NMR studies of alkali silicate glasses, J. Non Cryst. Solids 113 (1989) 253.

[63] J. F. Stebbins, Identification of multiple structural species in silicate glasses by ^{29}Si NMR, Nature 330 (1987) 465.

[64] H. Maekawa, T. Maekawa, K. Kawamura, T. Yokokawa, The structural groups of alkali silicate glasses determined from ^{29}Si MAS-NMR, J. Non-Cryst. Solids 127 (1991) 53–64.

[65] R. W. Schurko, C. M. Widdifield, Understanding chemical shielding tensors using group theory, mo analysis, and modern density-functional theory, Concepts in Magn. Reson. A 34 (2) (2009) 91–123.

[66] F. A. L. Anet, D. J. O'Leary, The shielding tensor. i. understanding its symmetry properties., Concepts in Magn. Reson. 3 (1991) 193–214.

[67] R. K. Harris, E. D. Becker, S. M. C. D. Menezes, P. Grangerd, R. E. Hoffman, K. W. Zilm, Further conventions for NMR shielding and chemical shifts, IUPAC recommendations 2008, Inorg. Chem. 3 (2008) 41–56.

[68] E. R. Andrew, Rotational narrowing of nuclear magnetic resonance spectra, Arch. Sci. 12 (1959) 103–108.

[69] E. R. Andrew, A. Bradbury, R. G. Eades, Removal of dipolar broadening of nuclear magnetic resonance spectra of solids by specimen rotation, Nature 183 (1958) 1802–1803.

[70] I. J. Lowe, Free induction decays of rotating solids, Phys. Rev. Lett. 2 (1959) 285–287.

[71] A. Samoson, E. Lippmaa, Sychronized double-rotation NMR spectroscopy, J. Magn. Reson. 84 (1989) 410.

[72] A. Samoson, E. Lippmaa, 2D NMR nutation spectroscopy in solids, J. Magn. Reson. 79 (2) (1988) 255–268.

[73] A. Samoson, E. Lippmaa, A. Pines, High resolution solid-state NMR. Averaging of second-order effects by means of a double-rotor, Mol. Phys. 65 (1988) 1013.

[74] H. Eckert, Structural characterization of noncrystalline solids and glasses using solid state NMR, Prog. NMR Spectroscopy 24 (1992) 159.

[75] A. Bax, N. M. Szeverenyi, G. E. Maciel, Correlation of isotropic shifts and chemical shift anisotropies by two-dimensional Fourier-transform magic-angle hopping NMR spectroscopy, J. Magn. Reson. 52 (1983) 147.

[76] Z. H. Gan, High-resolution chemical-shift and chemical-shift anisotropy correlation in solids using slow magic-angle spinning, J. Am. Chem. Soc. 114 (21) (1992) 8307–8309.

[77] W. T. Dixon, Spinning-sideband-free and spinning-sideband-only NMR spectra in spinning samples, J. Chem. Phys. 77 (1982) 1800.

[78] O. N. Antzutkin, S. C. Shekar, M. H. Levitt, Two-dimensional sideband separation in magic-angle spinning NMR, J. Magn. Reson. A 115 (1995) 7–19.

[79] M. Mehring, High Resolution NMR Spectroscopy in Solids, Vol. 11, Springer-Verlag, Berlin, 1983.

[80] P. J. Grandinetti, J. H. Baltisberger, A. Llor, Y. K. Lee, U. Werner, M. A. Eastman, A. Pines, Pure absorption-mode lineshapes and sensitivity in two-dimensional dynamic angle spinning NMR, J. Magn. Reson. A 103 (1993) 72–81.

[81] H. Y. Carr, E. M. Purcell, Effects of diffusion on free precession in nuclear magnetic resonance experiments, Phys. Rev. 94 (1954) 630–638.

[82] S. Meiboom, D. Gill, Modified spin-echo method for measuring nuclear relaxation times, Rev.Sci.Instrum 29 (1958) 688.

[83] K. E. Vermillion, P. Florian, P. J. Grandinetti, Relationships between bridging oxygen ^{17}O quadrupolar coupling parameters and structure in alkali silicates, J. Chem. Phys. 108 (17) (1998) 7274–7285.

[84] T. M. Clark, P. J. Grandinetti, P. Florian, J. F. Stebbins, An ^{17}O NMR investigation of crystalline sodium metasilicate: Implications for the determinations of local structure in alkali silicates, J. Phys. Chem. B 105 (2001) 12257–12265.

[85] T. M. Clark, P. J. Grandinetti, P. Florian, J. Stebbins, Correlated structural distributions in silica glass, Phys. Rev. B 70 (2004) 064202–1–8.

[86] T. M. Clark, P. J. Grandinetti, Factors influencing the ^{17}O quadrupole coupling constant in bridging oxygen environments, Solid State NMR 16 (2000) 55–62.

[87] T. M. Clark, P. J. Grandinetti, Relationships between bridging oxygen ^{17}O quadrupolar coupling parameters and structure in germanates, J. Non-Cryst. Solids 265 (2000) 75–82.

[88] T. H. Sefzik, T. M. Clark, P. J. Grandinetti, A computational investigation of ^{17}O quadrupolar coupling parameters and structure in alpha-quartz phase GeO_2, Solid State NMR 32 (2007) 16–23.

[89] T. M. Clark, P. J. Grandinetti, Calculation of bridging oxygen ^{17}O quadrupolar coupling parameters in alkali silicates: A combined ab initio investigation, Solid State NMR 27 (2005) 233–241.

[90] T. M. Clark, P. J. Grandinetti, Dependence of bridging oxygen O-17 quadrupolar coupling parameters on Si-O distance and Si-O-Si angle, J. Phys. Condensed Matter 15 (2003) S2387–S2395.

[91] J. R. Cheeseman, G. W. Trucks, T. Keith, M. J. Frisch, A comparison of models for calculating nuclear magnetic resonance shielding tensors, J. Chem. Phys. 104 (14) (1996) 5497–5509.

[92] M. J. Frisch, G. W. Trucks, H. B. Schlegel, G. E. Scuseria, M. A. Robb, J. R. Cheeseman, J. A. Montgomery, Jr., T. Vreven, K. N. Kudin, J. C. Burant, J. M. Millam, S. S. Iyengar, J. Tomasi, V. Barone, B. Mennucci, M. Cossi, G. Scalmani, N. Rega, G. A. Petersson, H. Nakatsuji, M. Hada, M. Ehara, K. Toyota, R. Fukuda, J. Hasegawa, M. Ishida, T. Nakajima, Y. Honda, O. Kitao,

H. Nakai, M. Klene, X. Li, J. E. Knox, H. P. Hratchian, J. B. Cross, V. Bakken, C. Adamo, J. Jaramillo, R. Gomperts, R. E. Stratmann, O. Yazyev, A. J. Austin, R. Cammi, C. Pomelli, J. W. Ochterski, P. Y. Ayala, K. Morokuma, G. A. Voth, P. Salvador, J. J. Dannenberg, V. G. Zakrzewski, S. Dapprich, A. D. Daniels, M. C. Strain, O. Farkas, D. K. Malick, A. D. Rabuck, K. Raghavachari, J. B. Foresman, J. V. Ortiz, Q. Cui, A. G. Baboul, S. Clifford, J. Cioslowski, B. B. Stefanov, G. Liu, A. Liashenko, P. Piskorz, I. Komaromi, R. L. Martin, D. J. Fox, T. Keith, M. A. Al-Laham, C. Y. Peng, A. Nanayakkara, M. Challacombe, P. M. W. Gill, B. Johnson, W. Chen, M. W. Wong, C. Gonzalez, J. A. Pople, Gaussian 03, Revision C.02, Gaussian, Inc., Wallingford, CT, 2004.

[93] L. Le Page, L. D. Calvert, E. J. Gabe, Parameter variation in low-quartz between 94 and 298k, J. Phys. Chem. Solids 41 (1980) 721–725.

[94] G. N. Greaves, A. Fontaine, P. Lagarde, D. Raoux, S. J. Gurman, Local structure of silicate glasses, Nature 293 (1981) 611–616.

[95] G. N. Greaves, X-ray absorption spectroscopy, in: Glass Science and Technology, Vol. 4B, Academic Press, 1990, pp. 1–76.

[96] M. C. Eckersley, P. H. Gaskell, A. C. Barnes, P. Chieux, Structural order in a calcium silicate glass, Nature 335 (1988) 525–527.

[97] P. H. Gaskell, M. C. Eckersley, A. C. Barnes, P. Chieux, Medium-range order in the cation distribution of a calcium silicate glass, Nature 350 (1991) 675–677.

[98] P. Florian, K. E. Vermillion, P. J. Grandinetti, I. Farnan, J. F. Stebbins, Cation distribution in mixed alkali disilicate glasses, J. Am. Chem. Soc. 118 (1996) 3493–3497.

[99] J. F. Stebbins, Effects of temperature and composition on silicate glass structure and dynamics: Si-29 NMR results, J. Non Cryst. Solids 106 (1988) 359–369.

[100] M. A. Eastman, P. J. Grandinetti, Y. K. Lee, A. Pines, Double-tuned hopping-coil probe for dynamic-angle spinning NMR, J. Magn. Reson. 98 (1992) 333–341.

[101] Q. Shen, J. Faraway, An f test for linear models with functional responses, Statistica Sinica 14 (2004) 1239–1257.

[102] L. Pauling, The principles determining the structure of ionic crystals, J. Am. Chem. Soc. 51 (1929) 1010–1026.